UiT

THE ARCTIC UNIVERSITY OF NORWAY

Faculty of Science and Technology
Department of Physics and Technology

Beam and plasma properties downstream from positively biased source chamber

—

Sindre Osnes
FYS-3931 Master's Thesis in Space Physics - June 2017

University of Tromsø
Faculty of Science and Technology
Department of Physics and Technology

Fys-3931
Masters Thesis in Space Physics

Beam and plasma properties downstream from positively biased source chamber

Sindre Osnes

June, 2017

Abstract

We study the effect of changing the separation grid bias in a double plasma device from -50 V to the same bias as the anode in the source chamber, 115V on the plasma and beam parameters downstream in the target chamber.

Two different probes were used to analyze the downstream plasma. We used an RFEA-probe to obtain information about the ions, such as the ion energy distribution and we constructed a Langmuir-probe in order to measure the temperatures, densities and plasma potentials in the new configuration.

We performed measurements with the RFEA-probe for both configurations and found that the beam density is reduced by 80% at the higher pressures and that the induced background plasma potentials increases from 42 V to 104 V with a corresponding reduction of beam energy. We also found that the background plasma density increased twofold as a result of the change.

The Langmuir plasma potentials closely matched the beam potentials detected with the RFEA probe, rather than the detected plasma potentials, and this discrepancy indicates that the Langmuir plasma potentials are not accurate for the new configuration. Further the Langmuir probe measurements provided electron temperature measurements in the range of 2-5 eV at radial positions within the grid aperture, and densities ranging from $5 * 10^{15} m^{-3}$ at the lowest pressure to $9 * 10^{15} m^{-3}$ highest pressure at the 0 cm radial position.

It was also found that it is possible to detect an electron beam when the separation grid was biased at the anode potential. This beam has a peak energy that approaches the anode-cathode potential difference as the pressure decreases and can possibly represent a means of detecting how effective the discharge current from the filaments in the source is at ionizing the neutral argon atoms in the source. These electron beams were only visible at the far edge of the grid aperture.

Uneven structures in the radial density distributions of the ions beams were detected, with the largest ion beam densities being found at the far edge of the aperture. These increased densities are thought to be caused by an uneven distribution of filaments in the source. This uneven distribution also serves as a possible explanation as to why we only found the electron beam on the far side of the grid.

Acknowledgments

I would like to express my sincerest gratitude to Prof. Åshild Fredriksen for the help and support she has given me as my supervisor for this project.

I would also like to extend my thanks to engineer Inge Strømmesen and the guys working at the University of Tromsø workshop for the invaluable technical assistance they have provided over the course of this project.

I would also like to thank Njål Gulbrandsen for allowing me to re-purpose his Matlab code for analyzing RFEA-measurements.

I would further like to thank the Department of Physics and Technology for the opportunity they gave me in being able to do my masters.

Finally I would like to thank my family and friends for supporting me along the way and always pushing me to be better.

Sincerely
Sindre Osnes

Contents

Chapter 1

Introduction

Double plasma devices were invented by [Taylor et al., 1970, 1972] as a means to study low energy ion beams. The devices have since been utilized to examine a wide range of phenomena regarding both the formation and the effects of double layers [Hershkowitz, 1985].

The double plasma devices have been extensively used in the research of plasma instabilities [Chutia et al., 1991; Barrett and Greaves, 1989] and ion beams [Armstrong and Schrittwieser, 1991]. Plasma wave studies have also been studied using double plasma devices [Sato et al., 1975] and there have also been experiments performed with magnetized double plasma devices [Pierre et al., 1987].

The double plasma device here at UiT, Njord, has also been used for a variety of experiments, such as the ion vortice experiments of Pécseli et al. [1981] and the Langmuir ion beam diagnostics done by Weber et al. [1979].

We can thus clearly state that double plasma devices are useful in observing a variety of phenomena, and that they are very adaptable.

1.1 Motivation

The motivation for this project came from the fact that recent improvements in available spacecraft power system increasing the viability of electric propulsion systems on satellites and other spacecraft [Mazouffre, 2016].

The original intent of the project was to use the fact that the dc plasma source in Njord is similar to a gridded ion engine (GIE), or ion thruster, but without the neutralizer to simulate how the ion beam would evolve with

distance and induce a background plasma in the target chamber. This would in effect simulate the failure of the neutralizer.

1.2   Short circuit

Whilst we originally intended to study a modified ion thruster we were unable to complete our experiments for that configuration.

What we instead had to contend with was that after we had conducted some of our experiments, the RFEA measurements at an axial distance of 6 cm from the source, we experienced a short circuit between the grid separating the target and source chambers in Njord and the anode cage in the source. This meant that the grid was now biased at the anode cage potential.

This short circuit drastically changed the outlook of our experiments and we now had an additional component that differed greatly from the basic ion thruster described in Mazouffre [2016].

The aim of this study became as a result of this short circuit to compare the ion energy distributions of the differing grid configurations configurations so as to show the effect the grid has on the beam parameters. We also wanted to utilize the Langmuir probe to gather data on how the new beam configuration affected the distribution of the plasma parameters.

Chapter 2

Plasma production and transport

This chapter will introduce the method by which we produce plasma in the Njord double plasma device and the means by which we transport said plasma to the target chamber where the measurements are taken. Section 2.1 gives a brief introduction into which plasma sources currently available in the Njord-plasma device before going into more detail regarding the means by which our chosen source, the filament source, produces its plasma. The section further describes some of the parameters of general plasmas that will be measured using the probes described in chapeter 3. Section 2.2 will introduce how the plasma is transported from the source chamber to the target chamber of the device.

2.1   Plasma production

The Njord device has two main means of producing plasma. One of these sources is a helicon plasma source mounted on the gas flow inlet tube, and the other is electron emitting filaments situated in a source chamber on the other end of the vacuum chamber. The device also has the capability of producing a filament plasma in the target chamber, but this will not be utilized.

The helicon source in the device has been the main means of producing plasma in the Njord device in since its installation in 2006 [Tribulato, 2007] and has been extensively researched since its installation [Byhring et al., 2008; Fredriksen et al., 2010], but this will not be the plasma source that we

will use for this project.

The source that will be utilized for this project is the filament plasma source. This plasma source produces its plasma by means of a DC-discharge current provided by the emitting filaments and the potential difference between these filaments and the anode cage which provides the necessary energy for the emitted electrons to ionize the neutral gas in the source.

The emitted current is provided by the filaments through thermionic emission. Thermionic emission occurs when the thermal velocity of the electrons in a material provides the electrons in said material with enough energy to overcome the potential well that they are trapped in, Roth [1995]. The potential is equal to the work function, ϕ, and is illustrated in figure 2.1 [Roth, 1995] where the varying energies of the mobile electrons provides a range or "width" of already present potentials within the metal ϕ_m. This means that the total band depth is given $\phi_b = \phi + \phi_m$, which is the potential that must be exceeded for all the mobile electrons to be emitted. The emission of electrons, which requires that the most energetic electrons overcome the potential barrier ϕ eV is normally not satisfied at low temperatures < 1000 K [Roth, 1995].

The emitted electron current density is given by Richardsons law [Åge Skøelv, 1981; Roth, 1995] and is given by

$$J_R = A_G T^2 e^{-\frac{e\phi}{k_B T}} \tag{2.1}$$

where T is the temperature of the emitting filament,k_B is Boltzmann's constant, $e\phi$ is the minimum energy, in eV, to be added for an electron to be emitted at 0 K as provided by the work function and A_G is the emission constant of the material. A_G has been used to differentiate the parameter from surface area and ampere.

For tungsten the work function is $\phi = 4.5$ V [Davisson and Germer, 1922; Åge Skøelv, 1981] and the emission constant has been determined to be $A_G \approx 6.0 * 10^5 Am^{-2} K^{-2}$ [Lassner and Schubert, 1999; Åge Skøelv, 1981]. This gives us the plot seen in figure 2.2.

As the electrons are initially emitted they will create a space charge around the filaments that limits the emitted current density according to Child-Langmuir's law which is given by Hershkowitz [2005] as

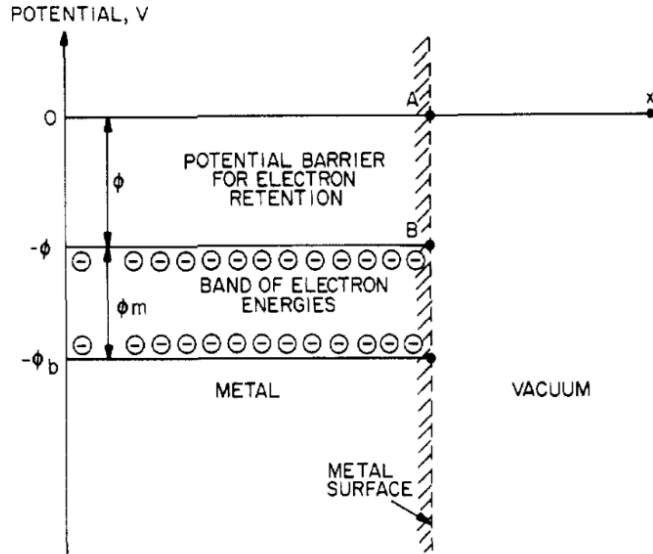$$J_C = \frac{4\epsilon_0}{9} \sqrt{\frac{2e}{m_e}} \frac{\Delta V^{3/2}}{x^2} \tag{2.2}$$

Figure 2.1: "The potential-istance diagram for electrons near the surface of a metal, indicated by the hatched line. The potential ϕ is the work function, the potential which an electron must acquire, from thermal energy or other sources, to leave the metal." Figure 5.1 in [Roth, 1995]

where ϵ_0 is the electric constant of a vacuum, m_e is the mass of an electron,ΔV is the anode-cathode voltage difference and x is the distance between them. In Njord the distance from the filaments to the anode cage is $x \approx 5$ cm, [Åge Skøelv, 1981]. Using a potential difference of 75 V we get $J_C = 0.606 Am^{-2}$ as the Child-Langmuir limit for the current. This would then be the limit for the current at the anode cage due to the electrons being accelerated from the filaments towards the anode cage.

As these electrons are accelerated towards the anode-cage they will have a probability of colliding with neutral gas and if the electrons have enough energy, the collision will cause ionization of the neutral argon atoms. This ionizing collision will produce an electron-ion pair that will be accelerated towards the anode cage and the filaments respectively due to the directional electric field caused by the anode cathode potential difference. As we now have two electrons being accelerated towards the anode cage instead of just one.
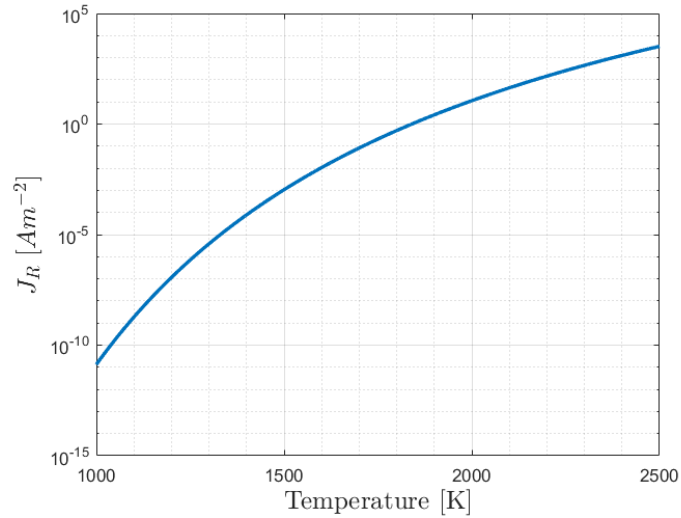
Figure 2.2: Plot of the thermionic emission current for a pure tungsten filament.

If either of these electrons now collide with a atom after it has attained a sufficient energy we will have another ionization event, further increasing the number of ions and electrons. This process is called avalanching as for each "generation" of ionizing collisions we increase the number of ions and electrons in the plasma thus essentially dragging the mass of the electrons along sort of like an avalanche.This is called a Townsend discharge, [Xiao, 2016], more specifically the α process. This process is illustrated in figure 2.3.
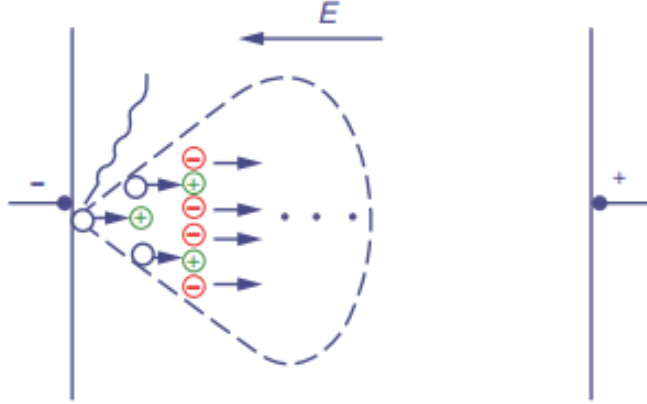
Figure 2.3: Image illustrating the α process, adapted from [Xiao, 2016, p. 49]

The probability of an actual collision between an electron and a neutral atom is governed by the density of the neutral gas, or rather the mean free path. The mean free path is the average distance traveled by a particle between random collisions with particle species i and is given by

$$\lambda_{mfp} = \frac{1}{\sigma_i n_i} \tag{2.3}$$

where σ_i is the collision cross section of the particle species and n_i is its density. For Argon atoms we approximate $\sigma_i \approx 10^{-19}$ [Phelps et al., 2000] and at our operating pressures between 10^{-4} mbar and 10^{-3} mbar we can assume a neutral gas density on the order of $n_{Ar} \approx 10^{18} - 10^{19}$. Given this we have a mean free path on the order of 1 m to 10 m. This means that most of the electrons emitted from the filaments will not ionize neutral atoms and will reach the anode cage unimpeded, [Åge Skøelv, 1981]. This will most likely be the case given that the mean free path exceeds the dimensions of the source chamber as described in section 4.1.

The electrons colliding with electrons colliding with the anode cage will have a possibility of releasing high energy sputtered electrons with an energy of $5 - 10$ eV [Åge Skøelv, 1981] leading to a bi-maxwellian velocity distribution. Osnes [2016] observed these hot electron distributions at a position far downstream and found that they generally had temperatures of < 5 eV with some measurements putting the temperature at high as 7.9 eV.

Åge Skøelv [1981] produced a plasma that had an electron density $n_e \approx 4.4 * 10^{14} m^{-3}$, an electron temperature of $T_e = 2.0eV - 2.5eV$ depending on the configuration and an ion temperature of $T_i = 0.33eV$ when there was a beam present. Similar plasma sources, [Taylor et al., 1972; Hollenstein et al., 1980] have produced plasmas with with varying electron temperatures $T_e \geq 1$ eV and ion temperatures of $T_i = 0.2eV$.

The velocity distribution of the particle species is given by their maxwellian velocity distribution

$$f(v) = n_s \left(\frac{m_s}{2\pi k_B T_s} \right)^{3/2} e^{-\frac{mv^2}{2k_B T_s}} \tag{2.4}$$

where n_s is the species density, m_s is the species mass and T_s is the species temperature. The thermal velocity is given as

$$v_{th,s} = \left(\frac{2k_B T_s}{m_s} \right)^{1/2} \tag{2.5}$$

and controls the width of the distribution, with a higher thermal velocity leading to a longer exponential tail. From the thermal velocity equation we see that an increased mass will reduce the thermal velocity whilst an increased temperature will increase it. From this we can tell that due to the relative mass differences as well as the fact that electrons are generally hotter than the ions that the thermal velocity of the electrons will far exceed that of the ions $v_{th,e} \gg v_{th_i}$.

A plasma is by it's very nature quasi-neutral, $n_i = n_e$, provided that the Debye length $\lambda_D \ll L$ where L is a characteristic length of of the system [Chen, 1984]. The Debye length of a plasma is given by

$$\lambda_D = \left(\frac{\epsilon_0 k_B T_e}{ne^2} \right)^{1/2} \tag{2.6}$$

and for our plasma $\lambda_D < 1$ mm. This is much smaller than any characteristic length L of our system, thus our plasma should be quasi-neutral.

In order to maintain that quasi-neutrality the fluxes of ions and electrons from the bulk plasma to the walls, the filaments and the anode cage has to be balanced. In order for this to be the case the bulk plasma must attain a potential that will slow the electrons heading towards the walls, or other "deposit" locations and accelerate the ions. This is due to the difference in

thermal velocity from the ions to the electrons. This potential will be positive with regards to the anode potential [Åge Skøelv, 1981]. The only disparity in the ion and electron fluxes out of the plasma will be the current inserted into the plasma from the filaments, i.e the emitted or discharge current.

2.2 Plasma transport

This section aims to explain the theory behind the transportation of plasma from the source chamber to the target, or measurement, chamber. The concept of double layers and beams will also be introduced. We further state that we will not be producing any plasma in our target chamber except for secondary ionization due to ionizing collisions from the plasma streaming from the source.

Hershkowitz [1985] defines double layers in a plasma as "Regions of non neutral plasma which resemble standing laminar electrostatic shocks", with reference to Montgomery and Joyce [1969], and provides a further definition when looking at axial potential profiles, figure 2.4, where he defines the presence of parallel charge sheaths to be a necessary condition for a plasma structure to be considered a double layer and not a sheath.
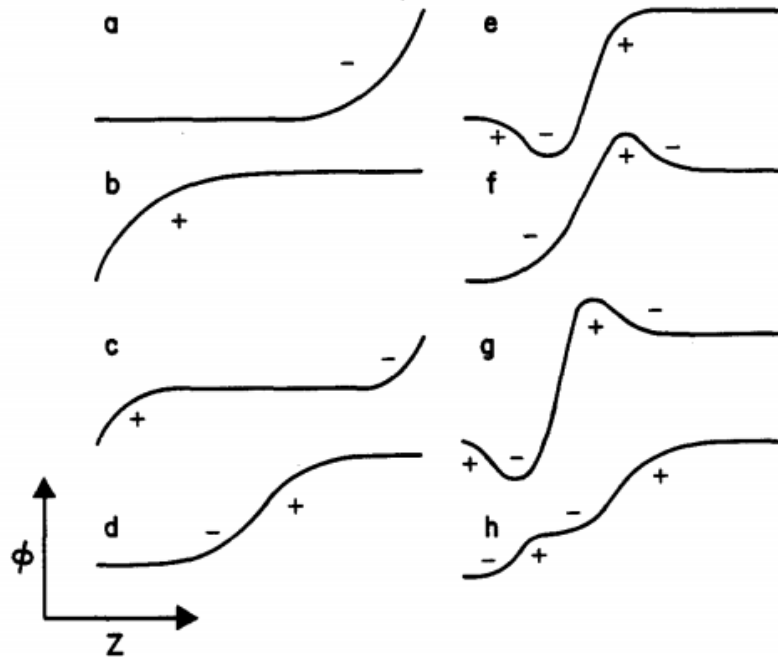
Figure 2.4: "Schematic of a variety of axial profiles which correspond to identical potential differences applied to system boundaries. The designated structures (a,b, c) are usually called sheaths while the remainder are called double layers because of the presence of parallel charge sheets as indicated by + and -. h is referred to as a stairstep double layer." Fig 1. in Hershkowitz [1985]

Under normal operations of the Njord double-plasma device such as in [Åge Skøelv, 1981], and in similar devices [Taylor et al., 1972]. We have the grid separating the plasma populations negatively biased so as to electrically isolate the two electron populations and allow the free flow of ions across the grid. This leads to a potential structure that is similar to figure 2.4e with the negative dip being centered on the axial position of the grid. The two plasmas containing distinct populations is what leads to this being called a double-plasma device, we simply have two different plasmas, one in the target chamber and one in the source chamber.

In this configuration, negative separation grid, we will get a beam of ions from the high potential side to the low potential side as seen in figure 2.5.
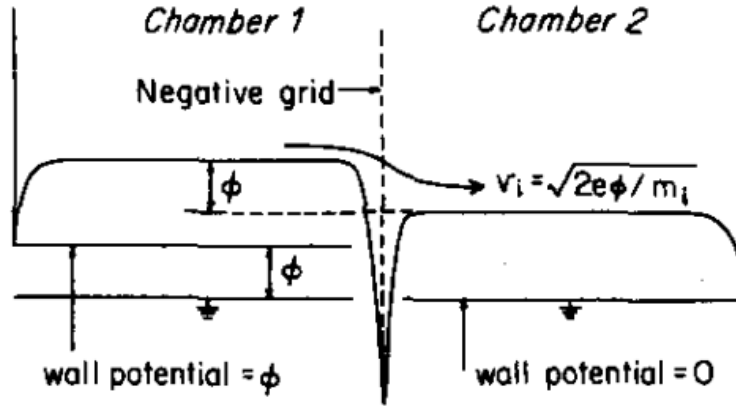
Figure 2.5: "Potential profiles in the two chambers showing how a beam of ions can be produced from a differential potential ϕ" [Taylor et al., 1972, p. 1677].

This ion beam that is produced will have a directional component to its velocity generated by the difference in potential between the two plasma plasma populations in the high to low potential direction with its velocity being given by:

$$v_b = \sqrt{\frac{2e\phi}{m_e}} \tag{2.7}$$

Which due to there not being produced any filament plasma in the target chamber to drive the plasma potential in the target chamber will be from the source chamber and into the target chamber.

In the configuration that we ended up with following the short-circuit described in chapter 1 we no longer have a negatively biased grid with respect to ground, instead we have a grid that is a part of the anode cage and that is thus biased at the anode potential. This leads to a potential structure that might be more in line with structure 2.4d or h, although structure e might still be a possibility, just not with such an extreme negative dip as we would see normally, figure 2.5.

We know from the condition of quasi-neutrality that the plasma in the source will have a positive potential with respects to the anode potential. We also know that as the grid is no longer negatively biased it will pose no barrier to electrons traveling to one plasma or the other bar the potential

drop from the plasma to the grid/anode.

From these fact we can deduce a few probable behaviors of our new plasma transport. We will most likely see some "communication" between our plasmas leading to the plasma potential and other parameters being more equalized between the two plasmas. We will as a result of this most likely get less ion beam energy, which is a function of the potential drop between the plasmas, equation 2.7. And as the separation grid is now a part of the anode cage we will have some of the electrons being accelerated from the filaments reaching the separation grid, and due to the grid having a transparency of 50%, we might get populations of accelerated electrons into the target chamber. How these parameters can be measured will be explained in the next chapter.

Chapter 3

Probe theory

This chapter aims to introduce the basic theory behind the probes utilized and to provide the equations needed to perform the calculations necessary to extract the plasma parameters from the measurements. Section 3.1 will introduce the Langmuir probe theory and detail some of the probes uses and limitations, whilst section 3.2 will do the same for the RFEA probe.

3.1   Langmuir probe theory

Langmuir probes is one of the simplest, if not the, simplest way to measure a plasma [Chen, 2003]. In general a Langmuir probe is a piece of conducting metal that is placed in the plasma and has a voltage applied to it. The current collected by the probe at various voltage biases is then what provides us with what is called the current-voltage or I-V curve, although some authors use the term characteristics instead, [Godyak et al., 2002; Sabadil et al., 1988]. The probes come in a variety of shapes, from simple wires to planar probes, and configurations from single probe configurations to multiple probes [Chen, 2003]. Langmuir probes provide a means of measuring the plasma density, n,(given the quasi-neutral nature of plasma), electron temperature, T_e and plasma/space potential V_S. We are however unable to measure the ion temperature.

There are 3 primary regions to a Langmuir I-V curve, the ion saturation region, the transition region and the electron saturation region. In order to be able to extract data from the I-V curve we have to know what the different regions of the I-V curve represents in terms of what influences the

different regions. Figure 3.1 provides an idealized I-V curve and will serve as the reference used when explaining the regions.
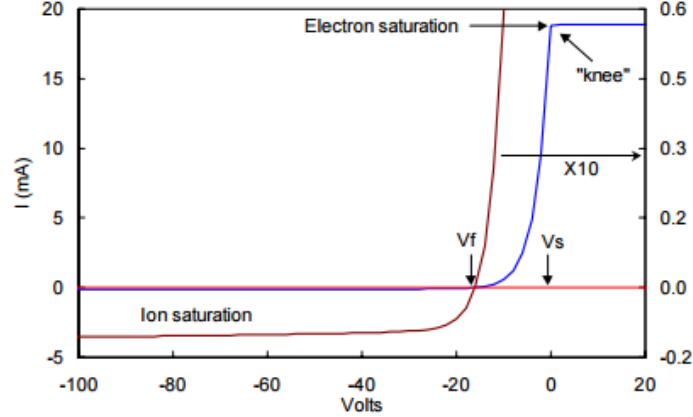

Figure 3.1:   "An idealized I-V curve where the left curve is expanded 10 times." Plot from [Chen, 2003, p. 2]

The ion saturation region is the region where the potential is sufficiently negative with respects to the plasma potential that the collected current is dominated by ions and the increase in magnitude of the current collected in this region is caused by the expansion of the current sheath. This region is the region to the left of the floating potential V_f which is defined as the potential at which the collected electron current equals the collected ion current $I_e = I_i$.

The electron saturation region is governed by the same principles as the ion saturation region, only with the potential exceeding the plasma potential V_S. Due to the relative difference in masses the electron saturation current is expected to be > 200 times larger than the ion saturation current, I_{sat}, [Chen, 2003].

The transition region is the region bounded by V_f and V_S, and is characterized by an exponential increase in current if the electrons are maxwellian, equation 2.4. The electron current is given by: The collected electron current can also be written as

$$I_e(V) = -Ae \int_{v_{m}in}^{\infty} f(v)v dv \qquad (3.1)$$

Where $v_{m}in$ is the minimum velocity needed to reach the probe given the

potential difference between the probe and the background plasma, A is the exposed probe area and $f(v)$ is the velocity distribution.

The velocity constraints take the form

$$
\begin{aligned}
v_{min} &= 0 & V_P > V_S \\
v_{min}^2 &= -2e(V_P - V_S)/m, & V_P < V_S
\end{aligned}
\tag{3.2}
$$

due to the kinetic energy the electron needs to obtain to break through the barrier set by the potential difference.

If a maxwellian distribution is assumed the electron currentis given by Chen [2003]:

$$
I_e = I_{es}exp\left[e(V_P - V_S)/k_B T_e\right]
\tag{3.3}
$$

where

$$
I_{es} = \frac{eAn_e\bar{v}}{4} = en_e A \left(\frac{k_B T_e}{2\pi m_e}\right)^{1/2}
\tag{3.4}
$$

Where I_{es} is the saturation current at V_S, and V_P is the probe potential.

This means that a semi-logarithmic plot of the transition region should be a straight line, from equation 3.3, with a gradient of $1/T_{e,eV}$ given that $T_{e,eV} = k_B T_{e,K}/e$. This gives us the means by which we can calculate the electron temperature. Solving equation 3.4 for n_e we get the following equation:

$$
n_e = \frac{I_{es}}{eA}\left(\frac{2\pi m_e}{k_B T_e}\right)^{1/2}
\tag{3.5}
$$

Thus the temperature can also be used for calculating the densities. In this thesis we have assumed a maxwellian velocity distribution, but non-maxwellian approaches has been utilized in other works, particularly for rf plasmas [Godyak et al., 1993].

Before we can obtain a good fit for the electron temperature in the semi-log plot of the transition region we will have to subtract the ion saturation current which is done by obtaining a linear fit to the I-V cure as far to the negative side of the curve as possible and extrapolating this out and subtracting it. Once this is done we should only have the electron current remaining. Plotting the logarithm of the electron current we now take the slope and use the inverse as the value for T_e.

Figure 3.2 shows the classical approach to obtaining the plasma/space potential by using the crossing point of the temperature and electron saturation current fits in the semi-log plot of the I-V curves.
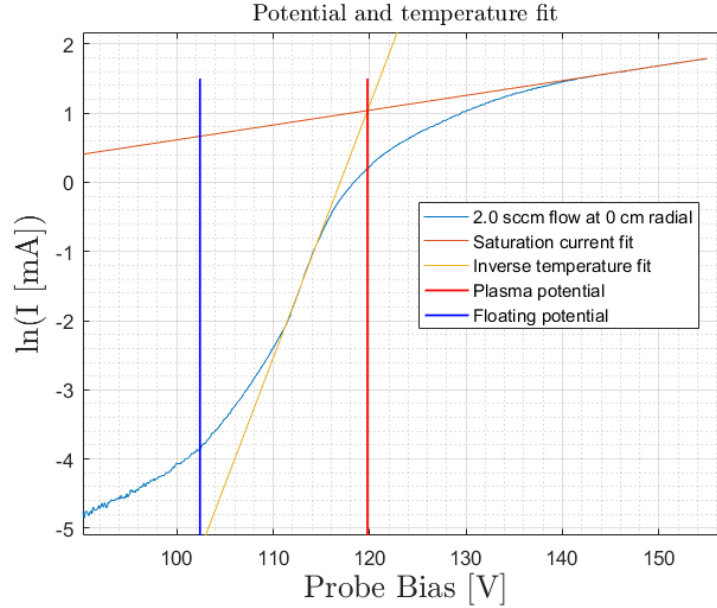
Figure 3.2: Example of obtaining the plasma potential using a linear fit for the inverse of the electron temperature, in eV, and a fit for the electron saturation current. The deviation from the temperature fit close to the floating potential is indicative of an additional hot electron distribution being present.

Chen [2003] presents us with a couple other methods that can be used to determine the plasma potentials, such as the maximum of the derivative and from the Bohm current criterion giving $V_f = V_S - \frac{k_B T_e}{2e} \ln\left(\frac{2m_i}{\pi m_e}\right)$. We will however stick to the classical approach for 2 main reasons:

Reason 1 is that, as can be seen in section 6.2.1 the derivative of the I-V curves does not have always have a distinct maximum. This means that we will not be able to accurately determine the plasma potential from the derivatives, thus invalidating that method.

The second reason we will stick to the classical approach is that we. as can be seen from figure 3.2 have high temperature electron populations present. The effect these populations has is that they can cause the floating potential to be more negative, thus extending the transition region.

The temperature of the hot electron populations, such as those produced by the sputtering mentioned in section 2.1, can be obtained by taking a

second linear fit in the part of the transition region closer to the floating potential, as illustrated in figure3.3.
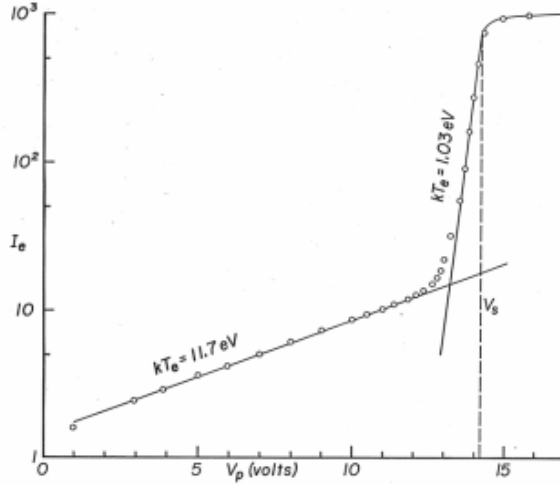

Figure 3.3: Semilog plot of I-V curve of a bi-maxwellian electron distribution [Chen, 2003, p. 37]

The presence of electron beams may also be detected using Langmuir probes [Chen, 2003]. These beams present themselves in the form seen in figure 3.4 and are the result of accelerated electrons with a directional velocity in addition to their thermal velocity. Their velocity distribution can be given by a drifted 1-dimensional maxwellian velocity distribution. in the form:

$$f(v) = n_s \left(\frac{m_e}{2\pi k_B T_b} \right)^{1/2} e^{-\frac{m(v-v_b)^2}{2k_B T_b}} \tag{3.6}$$

where the subscript b refers to the beam, [Chen, 2003]. The critical velocity that the electrons need to have in order to overcome the potential drop is given by the energy balance equation

$$\frac{1}{2}mv_c^2 = -e(V_p - V_S), \qquad v_c = \left[-\frac{2e(V_P - V_S)}{m} \right]^{1/2} \tag{3.7}$$

We further know that the beam velocity will be the velocity at the midpoint of the distribution and is present thermal velocity of the beam electrons will be given by their temperature as because of this we can calculate the critical velocity from the potential of the center of the distribution in figure 3.5.
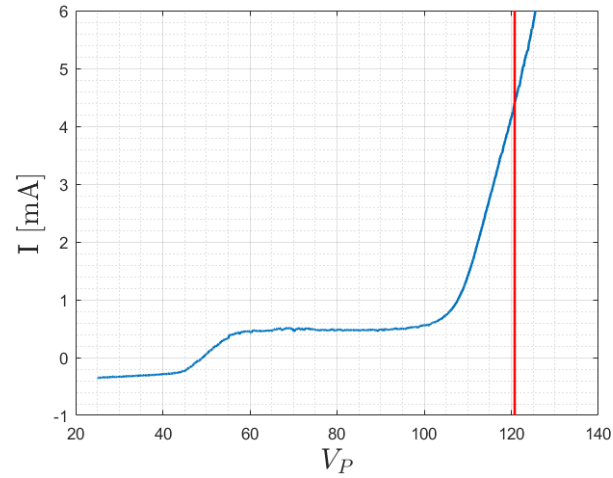
Figure 3.4:   I-V curve showing the presence of an electron beam at $V_P = 42V - 56V$. The red line is the plasma potential.
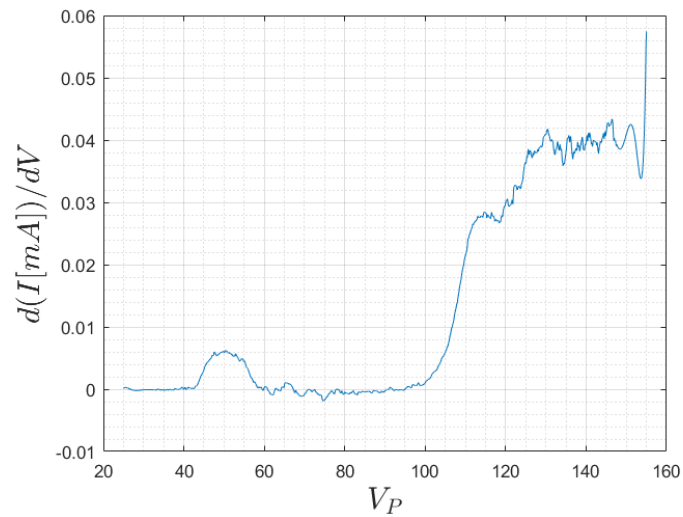

Figure 3.5:   Derivative of electron current from I-V curve in figure 3.4 showing the presence of an electron beam at with a peak in the distribution at $V_P = 50V$.

3.2 RFEA probe theory

The Retarding field energy analyzer, RFEA probe or as it is sometimes called, the ion energy analyzer, IEA, is a relatively simple probe used to measure the velocity distributions of the ions in a plasma [Stenzel et al., 1982]. The simplicity of the probes makes them a rather cost effective means of performing plasma diagnostics on ions [Aanesland et al., 2016].

The probes generally consist of multiple transparent grids spaced closely together that can be biased independently in order to perform certain functions based on their position and bias.

Figure 3.6 shows the functions of a 4 grid configuration, we do not count the floating front grid. The figure illustrates how the floating front grid will repel some electrons due to the potential drop relative to the plasma surrounding the probe, whilst the negatively biased grid 1, G1, repels the remainder through a further negative bias, for this reason G1 is called the repeller. The next grid, G2, is positively biased and as such only the sufficiently energetic ions will will pass through, although this is with respects to the plasma surrounding the probe due to the ions being accelerated through the sheath of the probe. The last grid, G3, serves to reflect the sputtered electrons back towards the collection plate, C, at the back of the probe to eliminate the effect this would have on the RFEA I-V curve.
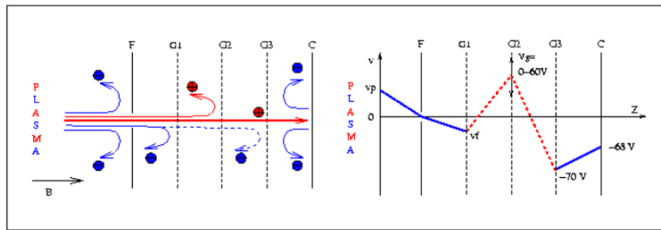

Figure 3.6: "The functions of the grids and their potentials." Figure 1 in [Aanesland et al., 2016]

G2 is what controls the flux to the probe as the potential is swept from below the plasma potential to above the potentials of any beams present. The voltage sweep leads to I-V curves such as the one in figure 3.7.

From these I-V curves we can extract information about the plasma potential, beam potential, densities and velocity distributions.

The potentials are found at the peak of the derivative in the respective regions, seen as the red and blue lines for plasma and beam potentials respectively.

As with the electrons in the Langmuir probe the ions have a minimum velocity needed to reach the collector, in this case set by the Discriminator potential. This can be written as; [Aanesland et al., 2016]

$$I_c(v_0) = Ae \int_{v_0}^{\infty} v f(v) dv \tag{3.8}$$

Here A is a constant based on both the aperture size of the analyzer and the transfission capabilities of the grids and $v_0 = \sqrt{2eV_g/m_i}$, where V_g is the grid potential and m_i is the ion mass. To change to an energy distribution we now utilize the relation $dE = m_i v dv$ and obtain [Aanesland et al., 2016].

$$I_c(eV_g) = \frac{Ae}{m_i} \int_{eV_g}^{\infty} f(\sqrt{\frac{2\xi}{m_i}}) d\xi \tag{3.9}$$

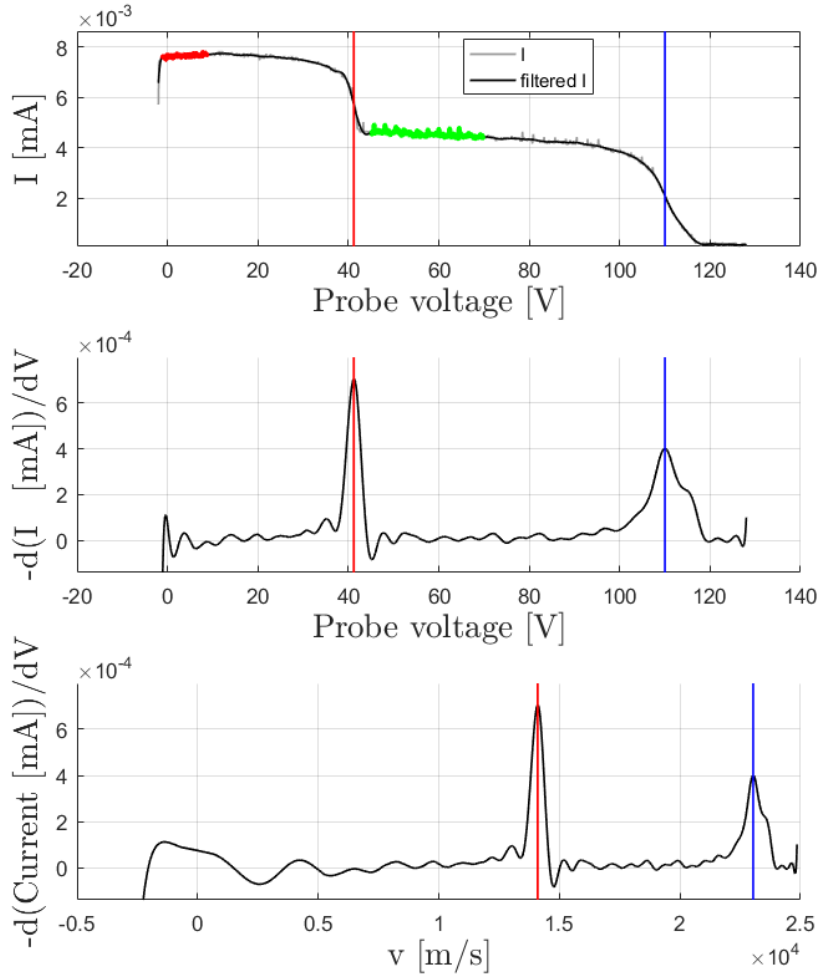ξ is the integration variable for the energy, and $eV_g = E$.

Figure 3.7: First plot is an example of an RFEA I-V blot with beam. Red vertical line is the plasma potential, and the blue line is the beam potential. The part of the plot marked in red is the saturation region, and the part marked in green is the start of the region where the background ions no longer have the necessary energy to pass the discriminator grid. Second plot is the derivative of the I-V curve, and the last image is the velocity distribution of the ions at the collector based on said derivative.

Equation 3.9 can be solved to obtain a measure for the ion velocity distribution as derived by Böhm and Perrin [1993].

$$f(v) = -A \frac{m_i}{e^2} \frac{dI_c(V_g)}{dV_g} \tag{3.10}$$

In terms of the beam parameters we have that the beam velocity is based on the potential difference between the beam potential and the plasma potential, i.e. the beam energy.

$$v_b = \sqrt{\frac{2e(V_b - V_S)}{m_i}} \tag{3.11}$$

We can also measure the densities of the beams by first expanding A as it has been used so far in this section, instead we will equate $A = AT^N$ where A is now the area of the aperture, N is the number of grids in front of the collector including the floating front grid and T is their transmission coefficient. The collection current for the beam is then simply a matter of equating the density of the beam and the speed at which it is moving to the area and the total transmission of the probe.

$$I_c(V_b) = eAT^N n_b v_b \tag{3.12}$$

For the plasma potential we simply use the saturation region $I(0)$ or as close as we can get to it and utilize the speed of sound of the ions, the speed the have at the edge of the sheath. This leads to

$$n_b = \frac{I_c(V_b)}{eAT^N v_b} \tag{3.13}$$

as the density for the beam ions and

$$n_i = \frac{I_0}{eAT^N c_S} \tag{3.14}$$

as the density based on the total flux, where c_S is the ion acoustic velocity given by:

$$c_S = \sqrt{\frac{k_B T_e}{m_i}} \tag{3.15}$$

If we integrate over the distribution below the rising point of the beam distribution, 100 V in figure 3.7 we should only get the flux due to the

background plasma, and we can then approximate the background density using 3.14 using the integrated current instead of the saturated current.

As the slope is quite steep at the potentials we will integrate over the energy distribution to approximate the total flux at each potential. This will allow us to better approximate the flux at the potential when the potentials are closer together, less beam energy as can be seen in The correlation between the ion flux and the beam density is further collaborated by Gulbrandsen et al. [2015].

Another approximation that we have to make is that we have to assume an ion temperature due to the temperature resolution of the RFEA being to large due to the large potential drops in the sheath [Miloch et al., 2011]. Gulbrandsen et al. [2015] further collaborates this with a direct comparison to Light induced florescence (LIF) measurements. We will thus assume an ion temperature of 0.2 eV for our experiments, based on similar plasma devices, [Taylor et al., 1972; Hollenstein et al., 1980].

Chapter 4

Eperimental hardware and probe construction

In this chapter we will describe the hardware used and premise of our experiment. The setup will be divided into 3 parts; Njord device and experimental parameter control systems, Langmuir probe, RFEA Probe. In addition the sections 4.2.2 and 4.2.3 contain information on what was actually done over the course of this project to construct the actual probes. Chapter 5 will cover the actual experiment procedure.

4.1   Njord plasma device

The Njord device consists of a stainless steel vacuum chamber that is 1.26 m long of 0.30 m radius cylinder with a half sphere dome, along with a gas flow port in one end and a pump port as shown in figure 4.1.

At the rear end from the dome, as seen from the inlet valve, a cylindrical anode cage has been inserted, allowing the source chamber to be isolated from the target chamber. This will also allow for double plasma operation as this is isolated from the target chamber, which is the remaining volume of the device. This cage is 30 cm long and electrically insulated, so that it can be biased with respect to the main chamber. The cage has, under ideal operation, 45 working filaments along the walls, however we do know that some of the filaments had failed prior to commencing our experiments. These filaments produce plasma in accordance with the principles discussed in section 2.1.

We know that prior to commencing the project some of the filaments had failed. We have postulated that one of the reasons for the failure of the filaments that there has been ten years since they were put in and that they might have oxidized somewhat in the meantime, thus decreasing their operative longevity. The failure of these filaments might induce some unevenness in the source, and it will put greater strain on the remaining filaments in order for them to keep up with the plasma production. This increased strain is the most likely cause for why the last remaining filaments finally failed.

A grid of diameter 20 cm is separating the target and source chambers, so that an ion or electron beam with a radius smaller than the radius of the main chamber can be created when a bias is applied. This bias is what form the premise of this work, as the short-circuit described in 1.2 forcibly changed the grid bias. The effects this had on the how the experiment was conducted will be elaborated in chapter 5.

4.1.1 Njord pressure control

Pressure control in Njord is done by varying the inflow of argon gas into the chamber. This is controlled by a computer with a LabView program. This is not to be confused with the one described in section 5.2, but is a separate system that, as stated, controls the inflow of argon gas into the vacuum chamber. The program also controls the vacuum pumps and the cooling systems for the helicon source. The chamber is pumped down by a Leybold 600 turbo pump in combination with a rotary pump, figure 4.1, to a base pressure on the order of $3 * 10^{-6}$mbar;
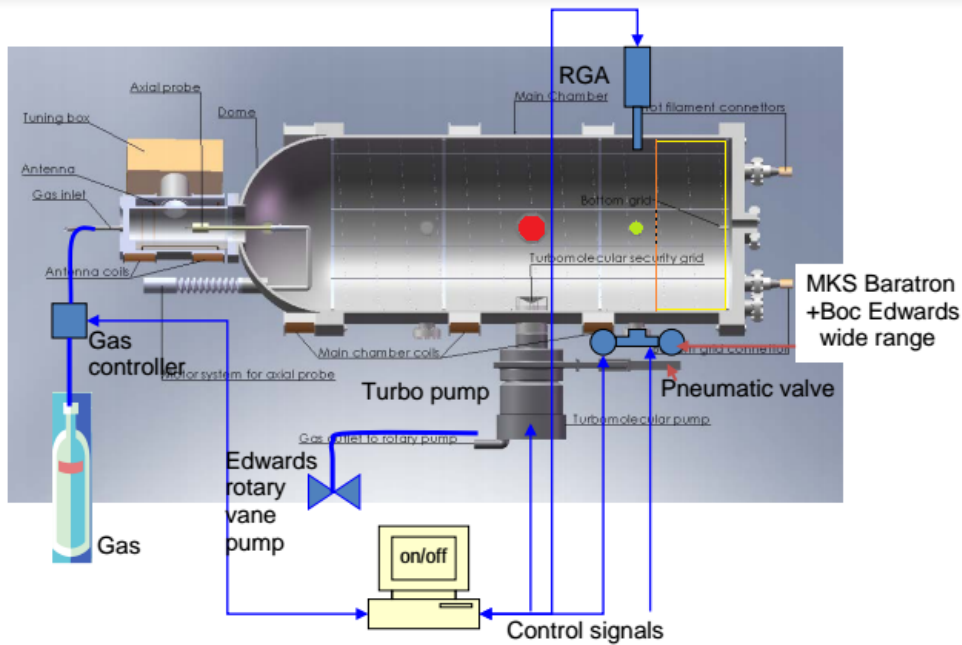
Figure 4.1: The physical structure of the Njord device gas control systems. The red port is the port used for the Langmuir experiment, the green port is the one used for the RFEA experiments and the position of the separation grid is indicated by the dashed orange line. The anode cage is outlined in yellow. Original image by Tribulato [2007]. Modified image courtesy of Åshild Fredriksen.

There are however some parameters affecting the pressure that are beyond the control of this LabView program, the most important of which is the leak rates into the system from sources other than the controllable gas flow. This sets the lower limit of the pressure, i.e. the base pressure.

There is also the heat generated by the plasma producing filaments. However both of these factors can be dealt with to an extent.

The leaks can be mitigated and in many cases prevented by adhering to engineering principles, such as tightening bolts opposite to each other so that the seals are evenly tightened.

The heat generated by the filaments can be dealt with by allowing the system to stabilize; this normally takes about 1 hour. This is generally not a problem however as the system has other considerations that require a longer

start-up time as described in 4.1.2.
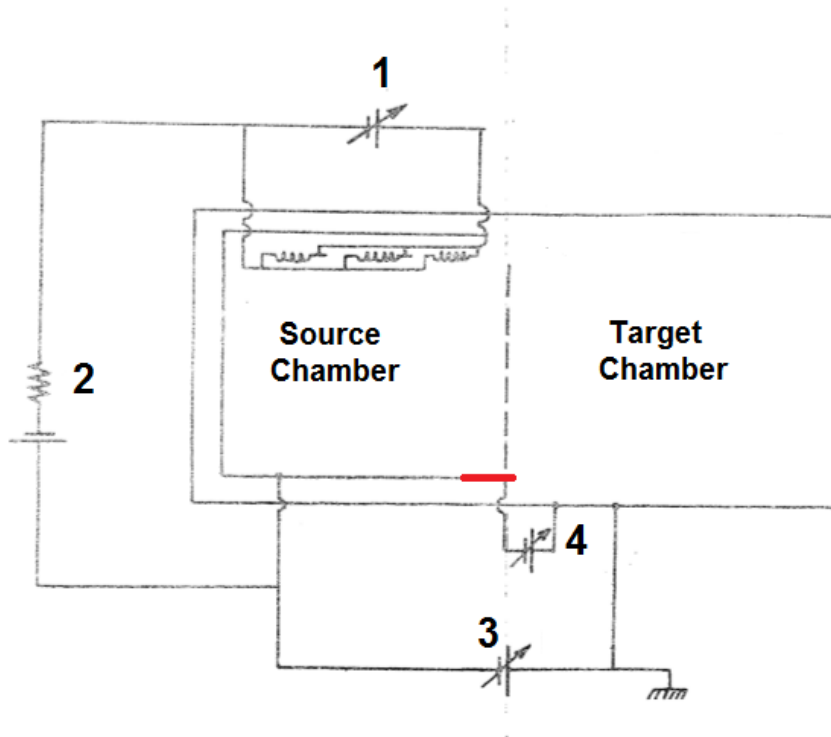
4.1.2 Plasma control and arcing

Figure 4.2: The electrical setup for the Njord device. Adapted from figure 2.3 in [Åge Skøelv, 1981].

Figure 4.2 shows the electrical circuit controlling the plasma production in the Njord device. In the figure power supply 1 provides the current through the filaments responsible for heating the filaments. Power source 2 sets the potential difference between the anode cage and the filaments and is thus responsible for setting the upper limit of the discharge current in accordance with the Child-Langmuir limit. The discharge current could be measured as the current trough this power supply. Power source 3 Biases the anode cage with respect to ground potential and is as a result of this responsible for controlling the plasma potential in the source chamber.

The last power supply, 4, is responsible for controlling the grid potential

and is biased with respect to ground. This power supply became superfluous once the short circuit between the grid and the anode cage happened, this short is indicated by the red line, as the grid potential was then controlled by power supply 3.

Upon start-up of the plasma, and especially as the discharge current increased we started to see a lot of arcing, particularly if the insertion rods had been in a position were they had been exposed to air between the time that the plasma was shut down for an extended period, e.g. overnight, and when it was started again.

This phenomenon had a tendency to go on for awhile, but it did decrease with time given that the insertion rods were inserted all the way, if this was not the case then we would have a resurgence of this effect as soon as the probe rods were sufficiently inserted. The effect of short extractions of the probe rods to re-position probes and start new measurement series was negligible in this respect, but we had brief resurgences if the measurement series was of such a length that the probe insertion rods were in an extracted, corresponding to a positive radial position, for extended periods of time. This was particularly the case in the first experiments as they had a much greater radial resolution and thus required more time to take the measurements.

The change in grid potential did not have an effect either reducing or increasing the time it took for the arcing events to subside. The time it took for the arcing to subside was generally on the order of 1.5-2 hours, but it could go on for longer in some cases, particularly when the vacuum had been broken.

4.2 Langmuir Probe

This section describes how a Langmuir probe was constructed and utilized in obtaining I-V curves at various axial and radial positions with regards to the center of the separation grid aperture. This probe was also utilized in the measurement of electrostatic fluctuations in the chamber, but this will be discussed in section 5.5.

4.2.1 Probe Design

Our first consideration when designing our probe was the fact that we would be unable to use the axial probe port on the inlet side of the vacuum cham-

ber, see figure 4.1. We also had the constraint of the opening of the port component, figure 4.3, used in the Langmuir experiments being to small with regards to its depth, which meant that this had to be removed each time we needed to take the probe out, this was because the 90° bend necessary for the probe positioning did not allow us to slip the probe in unless the component was removed as the opening behind it was slightly bigger and shallower. Due to the cobber seals used with the component being in short supply we needed a probe that could take several radial measurements without extracting the probe.
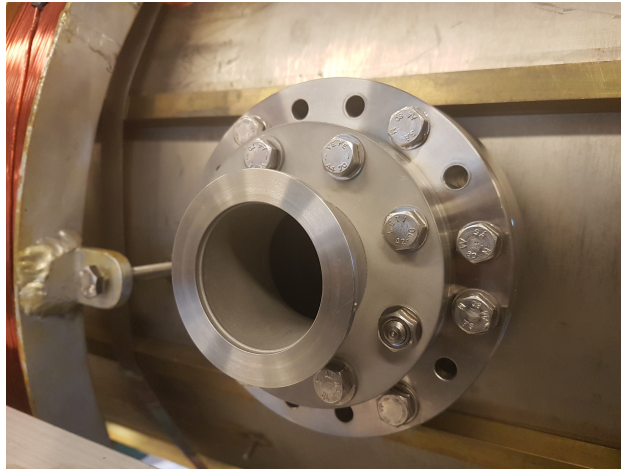
Figure 4.3: The port used to insert the Langmuir probe on Njord. The component restricting the opening of the port is the outer one.

Another constraint we had is the fairly low density of the plasma. Because of this the simple wire in a plasma [Chen, 2003] approach was not a viable option, instead a rectangular planar probe of 14 mm by 3 mm was constructed, and the design was then further modified so that several probes could be fitted on the same probe rod with an axial spacing of 2 cm.
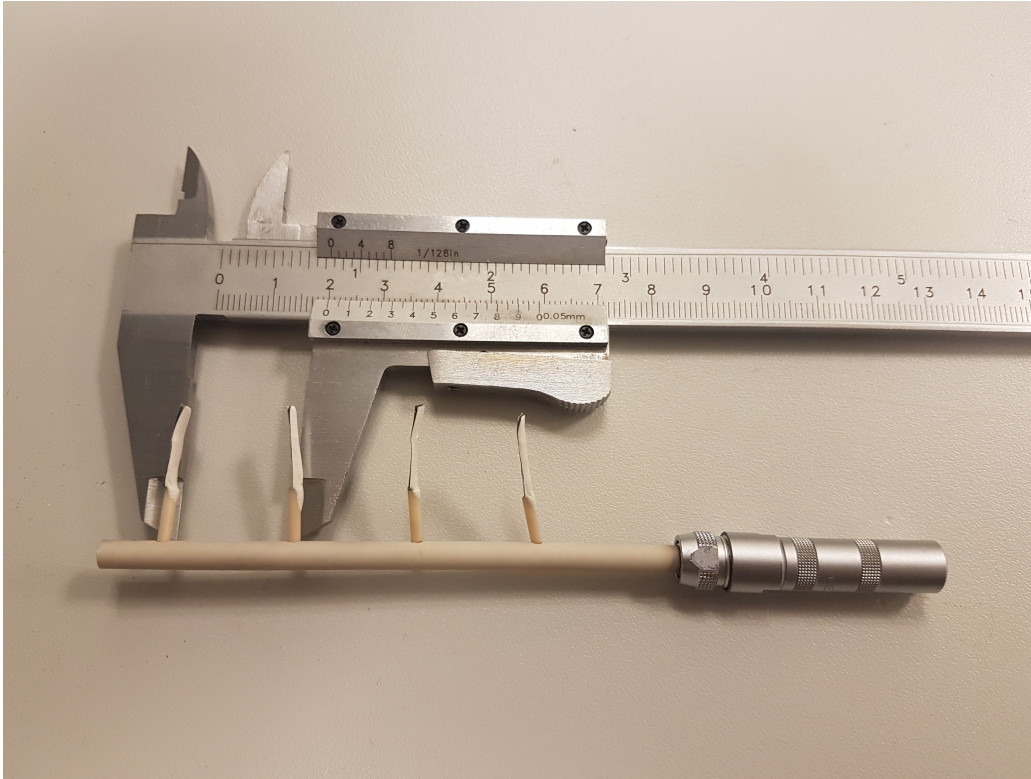
Figure 4.4: The Langmuir probe used in this project, with individual probe spacing set at 2 cm.

Each individual probe is made out of nickel conducting and has been isolated on the side meant to be facing away from the plasma source, down-stream. These probes apart from being spaced spaced 2 cmapart, figure 4.4, are also tilted slightly in order to reduce possible shadowing effects, as can be seen in figure 4.5.

The probes also have a short piece of thin ceramic tubing between the main ceramic rod of the probe and the probe plates so as to provide stability and increase the distance from the main probe rod, thus also providing the lever arm for the tilting of the probes. Theses tubes, and the wires that go through them were then inserted through holes drilled into the side of a hollow ceramic rod with an internal diameter large enough to feed 4 wires through. The excess ceramic rod beyond the first probe on the probe mount is there to allow the smaller ceramic tubes to have an anchor point as well
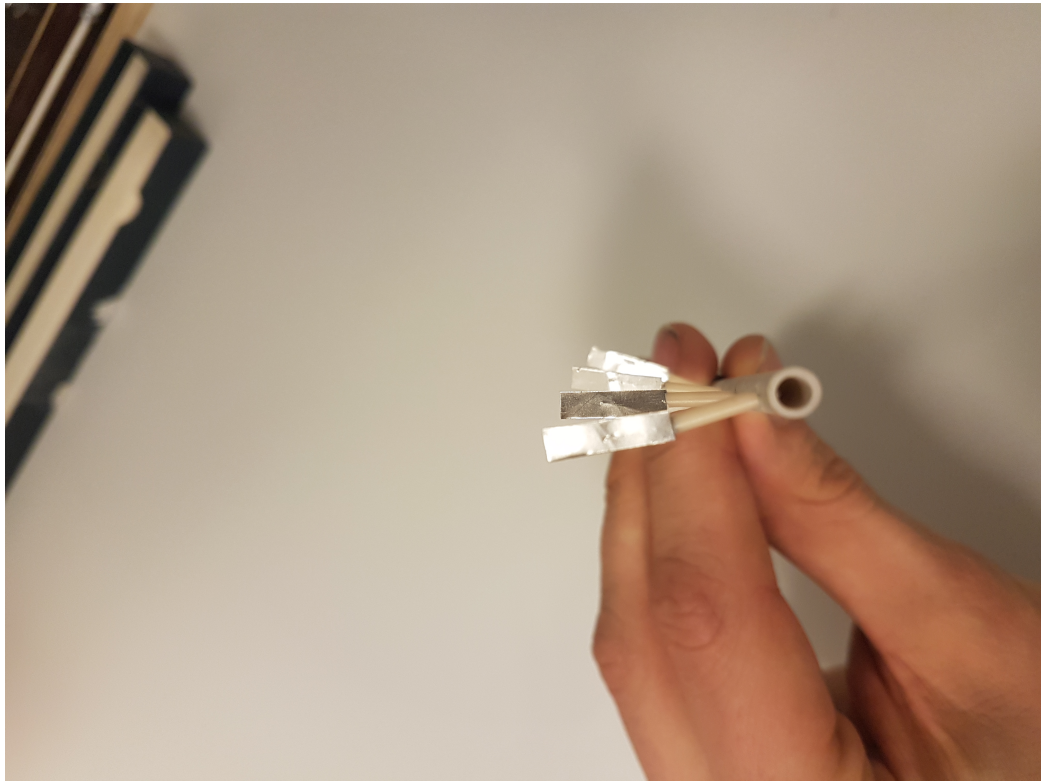
Figure 4.5: Front-facing profile of the Langmuir-probe with the individual probes at slightly different angles to minimize shadowing effects due to overlap.

as to ease repair if it should be needed, the end of the ceramic rod is then capped with a thin layer of ceramic adhesive to ensure that no plasma enters the rod and causes interference.

The main probe, the entire construct as seen in figure 4.4 is then mounted on a 90° "knee", seen in figure 4.6, in order to face the probes towards the plasma stream, and the axial position is controlled by the addition of the extension rods, 8 cm, 14 cm and 22 cm, seen in figure figure 4.6 alongside the "knee" component.

The lengths of the extension rods were chosen so that using the longest extension rod, 22 cm, the probe closest to the source would be 2 cm closer than the axial position that the RFEA-probe described in section 4.3, approx 6 cm. Thus the closest closest possible distance for the Langmuir probe was

4 cm.

Whilst the extension could have been made slightly longer, the design of the probe mount, with the excess ceramic on the front end, led to a real concern for the probe to scrape the separation grid if we went closer. Therefore the 22 cm,extension was the longest extension for the Langmuir probes. The 22 cm extension did however have a short-circuit on channel 1 of that extension which led to the 4 cm position being unavailable, and thus the 6 cm axial position was the closest we could get to the grid.

The 14 cm extension was designed so that there would be no overlap between the positions allowed by it and the positions allowed by the longer extension, whilst also providing a spacing of 2 cm between the probe tips on the two consecutive extension rods.

Similarly the 8 cm extension was designed to not allow overlap with the positions allowed by the probe when there is no extension. As a result there is overlap between the closest position for the 8 cm extension and the furthest position on the 14 cm extension.

The extensions thus allow for axial positions of 6 cm to 32 cm to be utilized with 2 cm separation between the distances. Radial distance is controlled using the insertion rod.

Figure 4.6: All the components that were made for this project to complement thee Langmuir probe. From right to left: 90° "knee" component, 8 cm extension rod, 14 cm extension rod and 22 cm extenstion rod.

4.2.2 Probe construction

In this section the work done to construct the actual Langmuir probes will be described.

The process started with drilling 4 holes spaced 2 cm apart in a ceramic rod using a Dremel Drill, whilst also leaving a distance of ceramic tubing between the furthest hole and the end of the rod, as per the design described earlier. The rod was then cut and ground down so that the distance between the closest probe and the center of the knee was 7 cm allowing for the furthest distance between separation grid and probe to be 32 cm. Using a shorter distance between the knee and the probe was not possible as the remaining room on the ceramic rod would not allow for it to be 2 cm shorter.

The ceramic tube was then fitted with a fastener to allow the Lemo-plugs to fit snugly on the end facing away from the source.

Four wires were then soldered onto the channels of a Lemo-plug, one for each channel, and isolated from each other using Teflon tape. The wires were then fed through the ceramic rod and made to extend through the individual holes along the rod. The positions were then confirmed with an ohmmeter. The exposed pieces of wiring were then stripped of their insulation and fitted with the smaller ceramic tubes.

The next step was to spot-weld the 3 mm by 14 mm plates onto the exposed wires using a Sunstone spotwelder. The welding was done so that the wires were connected to the side of the plate facing towards the plug and thus away from the plasma source.

This was then followed by the final step which was adding ceramic adhesive to the side of the probe facing the plug. The adhesive was then allowed to dry overnight before adding a second layer of adhesive the next day , as well as a final layer the day after that. The reason for adding several layers of adhesive is that a single layer is quite thin and thus very brittle.

4.2.3   Component construction

This section will describe the work done to construct the components needed for the operation of the Langmuir probes. These components include the extensions and the "knee".

The extensions were made by first cutting a piece of thin metal tubing into a length slightly shorter than the distance desired for the connector as a whole. This ambiguity is due to the fasteners not all being the same and as such the length contribution to the probe is slightly different. We then connected the Lemo-plugs to each end, one male plug, figure 4.8a, and one female plug, figure 4.8b, and measured the distance between the base of the male plug to the end of the female plug, as seen in figure 4.7. The lengths were then adjusted to fit the design requirements as described in section 4.2.1.
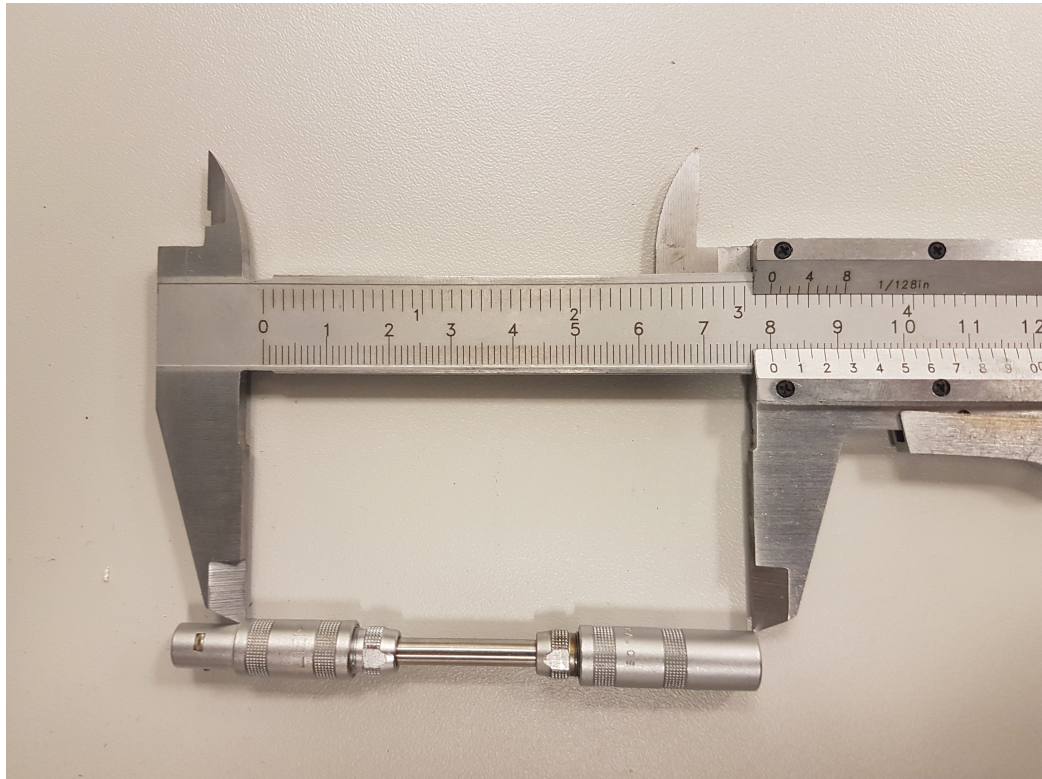
Figure 4.7:   An image showing how the length of the rods wee measured.

The side with the male plug then had wires soldered on to the plug, one for each of the four channels, and isolated. The wires were then threaded through the extension rod and the male plug was fastened to the metal tube of the extension rod again.

The wires on the other end were then cut to length and stripped of insulation at the tip in preparation for soldering. However before the soldering could commence the fastener on the female side of the extension had to be re-added because it would be impossible afterwards. The wires were then soldered onto the Lemo-plug on the female side and re-insulated, and the the plug was fastened. This process was the same for all 3 extensions.

The "knee" was fashioned in the same way only using the 90° component as the male plug, and adding a small piece of metal tubing to the female side of the component. Soldering and fitting the female plug follows the same procedure as described for the extension rods.

(a) A male Lemo-plug

(b) A female Lemo-plug

Figure 4.8: A figure with two subfigures

4.3 RFEA Probe

This section will describe the RFEA probe used in this project.

Figure 4.9: The RFEA probe used in this project.

The RFEA probe, figure 4.9, used in this experiment has a 3-grid setup with a single repeller and discriminator as shown in figure 4.10. The functions of the grids was described in section 3.2. The grids are housed in a ceramic housing and are sitting behind an aperture/front grid grid also seen in figure 4.10. The aperture of the RFEA probe has a diameter of 7 mm and all grids have a transparency of 50%.
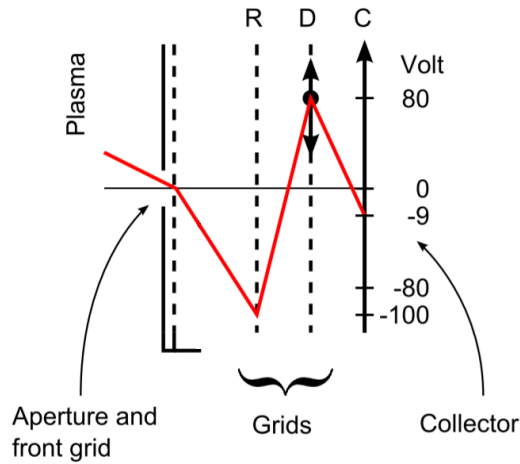
Figure 4.10: Illustration of the grid configuration used in our RFEA-probe. R is the repeller grid, D is the discriminator and C is the collector. Adapted from figure 3a in [Gulbrandsen et al., 2015]

The operation of this probe requires that the repeller is connected to a negative voltage source; we use -80V for our probe. The discriminator is connected to a battery bank with the possibility of choosing anywhere between 1 and 15 $9V$ batteries thus allowing for us to manipulate the horizontal translation of the resulting I-V curve. The battery bank is then connected to the output of the LabView computer, section 5.2, which controls the sweep voltage. Finally the collection grid is connected, via a 9V battery, to a measurement resistance with a measurement resistance of 100 kΩ. The measured signal is then sent to the input port on the LabView computer and stored.

Chapter 5

Experimental procedure

This chapter will explain in detail how the experiments were performed as well as the reasoning behind why they were performed as they were. The chapter will also explain the time-line of the experiments as understanding this time-line will be required in order to understand the restrictions under which certain parts of the experiments were performed.

5.1 Plasma control parameters

This section will detail the control parameters for the plasma production.

For this project all experiments were run with a $500mA$ discharge current from cathode filaments to the anode cage, this was kept constant by adjusting the current through the filaments as necessary, power supply 1 in figure 4.2.

We also applied a constant $115V$ potential difference between the anode and ground, power supply 3, and a $75V$ potential difference between the anode cage and the filaments, power supply 2. This means that the filaments had a potential of $40V$ relative to ground potential.

Further we operated with 3 different gas flows for our experiment with subsequently different pressures, see table 5.1.

Table 5.1: Table of flow values and measured pressures from the Boc
Edwards wide range pressure sensor.

Gas Flow	Pressure
1.5 sccm	$2 * 10^{-4} mbar \pm 10\%$
2.0 sccm	$5 * 10^{-4} mbar \pm 10\%$
2.5 sccm	$9 * 10^{-4} mbar \pm 10\%$

The final control plasma control parameter we have is the separation grid
potential which governs plasma transportation. It is for this parameter the
time-line of the experiments becomes important.

Table 5.2: Time-line of experiments with regards to separation grid short
circuit.

	Post short
RFEA-measurements	RFEA measurements
	Langmuir I-V measurements
	Langmuir turbulence measurements

Before the short circuit happened we had carried out RFEA-measurements
with the probe facing upstream, and perpendicular to the stream, at the 6
cm axial position and with radial positions ranging from -12 cm to 18 cm,
with the negative side being the side furthest from the port used to insert
the probe, green port in figure 4.1. The measurements were taken with a 5
mm radial resolution, for the upstream facing measurements and with a 1
cm resolution for the perpendicular measurements.

After these measurements were taken we experienced the short circuit
and we were forced to re-plan our experiments as repairing the plasma source
would take at least one month, and the engineer responsible for the plasma
lab at UiT was unavailable, thus extending the repair time beyond the time
allotted to the project.

As can be seen in table 5.2 the majority of the experiments were done
post short-circuit. The procedure for these experiments will be described
in the following sections. A further note is that the filaments in the source
eventually failed, preventing us from acquiring additional data.

We will for the remainder of the paper call the pre short-circuit config-
uration the old configuration, which corresponds to a grid voltage of -50 V.

The post short-circuit configuration with a grid potential of 115 V will be called the new configuration.

5.2 LabView

This section is dedicated to providing a brief description of the LabView program that controls the collection of I-V curves for the Langmuir Probes and the RFEA measurements.

The LabView program has a few function and control parameters. The program allows the user to set the sweep voltage up to $\pm 65V$. It also allows you to set the number of ramp steps used in the sweep so you can control the resolution of your I-V plot. Further it allows you to set the number of samples it gathers for each of the ramp steps, thus affecting the noise contribution to the I-V curve. This is especially important when the signal strength is low to begin with. A higher number of samples averaged increases the the signal to noise ratio.

The system is not without it's faults however, as it induces a slight bias that one has to be corrected for, but this can easily be remedied by taking an I-V measurement without plasma in the chamber and subtracting this from the I-V curves obtained for the measurements.

5.3 RFEA measurements

As stated the RFEA-measurements we were the only ones were able to acquire before the short-circuit between the separation grid and the anode cage. Thus these measurements will serve as the indicator on what effect this has had on the transport of plasma from the source chamber into the target chamber. Further, due to the fact that an RFEA-probe is a far easier tool to use in order to discern ion beams in a plasma, this will be our main means of characterizing the beam conditions close to the separation grid.

The RFEA-measurments were taken at an axial distance of approx. 6 cm from the separation grid, using the green port in figure 4.1. The measurements were taken at all 3 gas flows and thus their corresponding pressures, section 5.1.

The radial probe positions utilized ranged from 2 cm outside of the separation grid aperture on the far end, with respects to the chamber port

utilized, to 8 cm outside the aperture on the nearside. This corresponds to the aforementioned radial positions of -12 cm to 18 cm.

The spatial resolution utilized in the upstream facing measurements was 0.5 cm in the old configuration and 2 cm in the new configuration. The main reason for the reduction in spatial resolution was that we were unsure as to the integrity of the source after the failure and we were as such inclined to reduce the resolution in order to ensure that we obtained some data. We also saw a reduction in the the time needed to wait between measurements as the probe spent less time in an extracted position, thus we had less arcing as explained in section 4.1.2.

We also obtained perpendicular RFEA measurements in the old configuration These were taken with a radial resolution of 1 cm.

Apart from this the parameters were all kept the same for both scenarios: The number of samples averaged per data point was 500+, on the condition was that the number of averages was to be increased to 1000 if large amounts of noise was detected and the sample had to be redone. The voltage sweep of the discriminator was $\pm 65V$, with a ramp step of $0.1V$ The discriminator was further positively biased by 72 V by the usage of 8 batteries from the battery bank described in section 4.3. The repeller was kept at a constant potential of $-80V$ and the collector was biased at -9 V due to the battery that was connected to it to draw the current.

The RFEA measurements were actually the last experiments to be performed in the new configuration as we wanted to be able to remove the Langmuir probe and reduce the arcing. This necessitated that the Langmuir measurements be performed first as changing the axial distance as well as removing the Langmuir probes required us opening a seal, which was one of the design constraints of the Langmuir probes, section 4.2.1.

The remaining filaments in the source failed during the start up procedure of the plasma source the day after the the upstream facing RFEA measurements were performed in the new configuration, thus making us unable to perform the perpendicular measurements in the new configuration.

5.4   Langmuir I-V measurements

The Langmuir I-V measurements were all taken in the new configuration using the probes described in 4.2.1.

The sweeps were taken with the applied bias potential at $90V \pm 65V$,

with the $90V$ center bias being enabled by using 10 $9V$ batteries in series in addition to the sweep voltage from the LabView computer. The measurement resistance used for the Langmuir I-V measurements was 100Ω.

The radial positions of the sweeps were at -10 cm, -5 cm, 0 cm, 5 cm, 10 cm, 14 cm and 18 cm positions, where the ∓ 10 cm positions corresponds to the far and near edge of the grid aperture respectively. The probe was at its deepest insertion at -10 cm.

Further the 4-probe configuration was used in conjunction with the extension rods to take the I-V measurements at the aforementioned radial positions at axial of 6 cm, 12 cm, 18 cm, 24 cm and 30 cm. This corresponds to using channels [2,1,4,4,3] in that order for the axial positions.

These measurements were used to determine the electron temperature of the plasma and its density at these locations in the measurement plane, as seen in chapter 6.

The measurements were repeated for all 3 gas flows.

5.5 Electrostatic fluctuation measurements

This section will cover the means by which we obtained a rudimentary overview of the electrostatic fluctuation in the plasma using an oscilloscope.

To obtain the fluctuation measurements we connected low pass low-pass RC-filters with a cutoff frequency of 133 kHZ to the channels of the oscilloscope and to the corresponding probe tips of the Langmuir probes.

We then set the oscilloscope to sample at a frequency of 500 kHz for 2 seconds in the AC-voltage setting. This was done for all four probe tips simultaneously giving us a total of 10^6 samples for each probe tip.

As this was done alongside the Langmuir measurements we we obtained samples for each 2 cm axial position possible, due to all extensions having been used to enable the Langmuir probe positions, and we got the measurements for the same radial positions as for the Langmuir I-V measurements. i.e. -10 cm, -5 cm, 0 cm, 5 cm, 10 cm, 14 cm and 18 cm positions, where the ∓ 10 cm positions corresponds to the far and near edge of the grid aperture respectively.

We will in this paper look at the standard deviation of the collected samples as a measure of the magnitude of the fluctuations present at each radial and axial position.

Chapter 6

Results

This chapter contains the experimental results gathered using the methods described in chapter 5. Section 6.1 focuses on comparing how the different grid configurations affect ion populations and the induced plasma potentials whilst section 6.2 focuses on how the electron population is distributed throughout our plasma using the new configuration.

6.1   RFEA results

This section will present the data collected for the different configurations with section 6.1.1 presenting the results for the old configuration and section 6.1.2 doing the same for the new configuration.

6.1.1   Old configuration

In order to be able to extract information from the data we had to filter the data. Figure 6.1, clearly shows the necessity of this filtering as it would otherwise be impossible to discern any data from the derivative due to the noise. As such we have employed a ninth order Savitzky–Golay filter on all RFEA measurements in order to deal with the noise. The Savitzky-Golay filter was chosen due to its ability to preserve the derivatives [Magnus and Gudmundsson, 2008]. This is also done for each derivative step in order to extract the data. The effects of this filtering can be seen in the derivative plot in figure 6.1 where we can actually see the ion energy distribution. Another point that makes analysis requiring derivative difficult is the low signal-to-

noise ratio at the lower pressures, particularly once you reach the edge of the beam, as seen in figure 6.2.
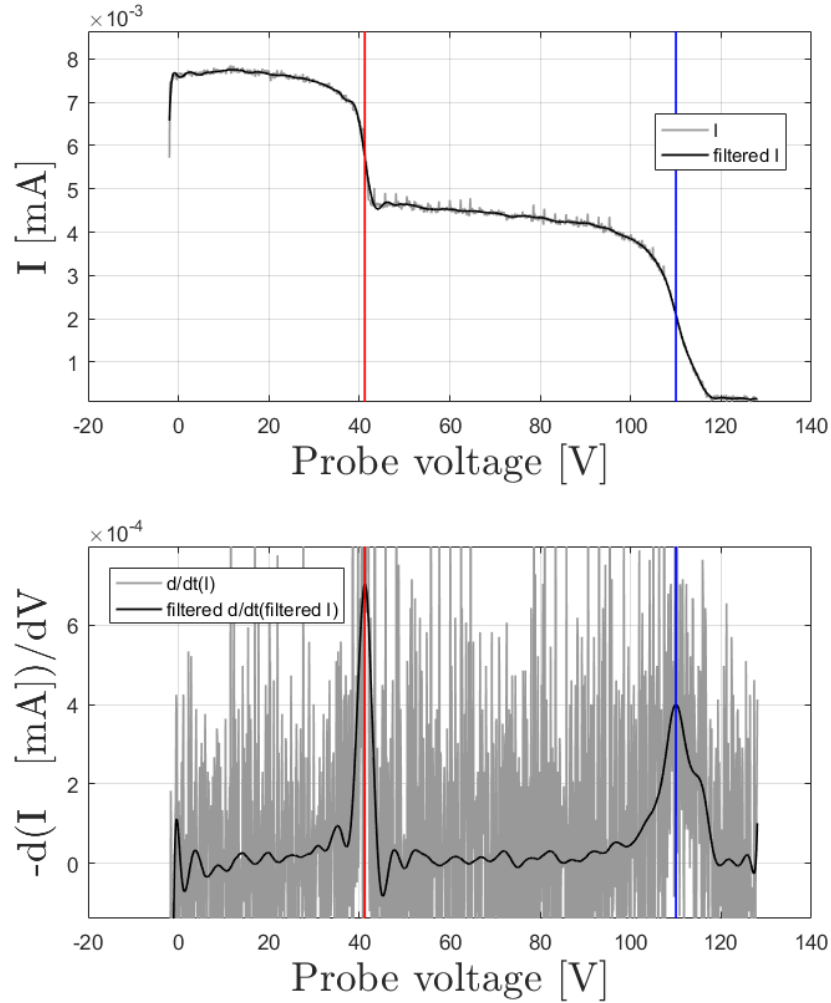
Figure 6.1: RFEA I-V curve obtained for the 2.5 sccm gas flow at the edge of the beam, 13 cm radial position. The red and blue lines represent the plasma and beam potentials respectively, obtained from the derivative in the lower image. The probe voltage is the discriminator voltage -9 V to account for the negative bias on the collector as illustrated figure 4.10.
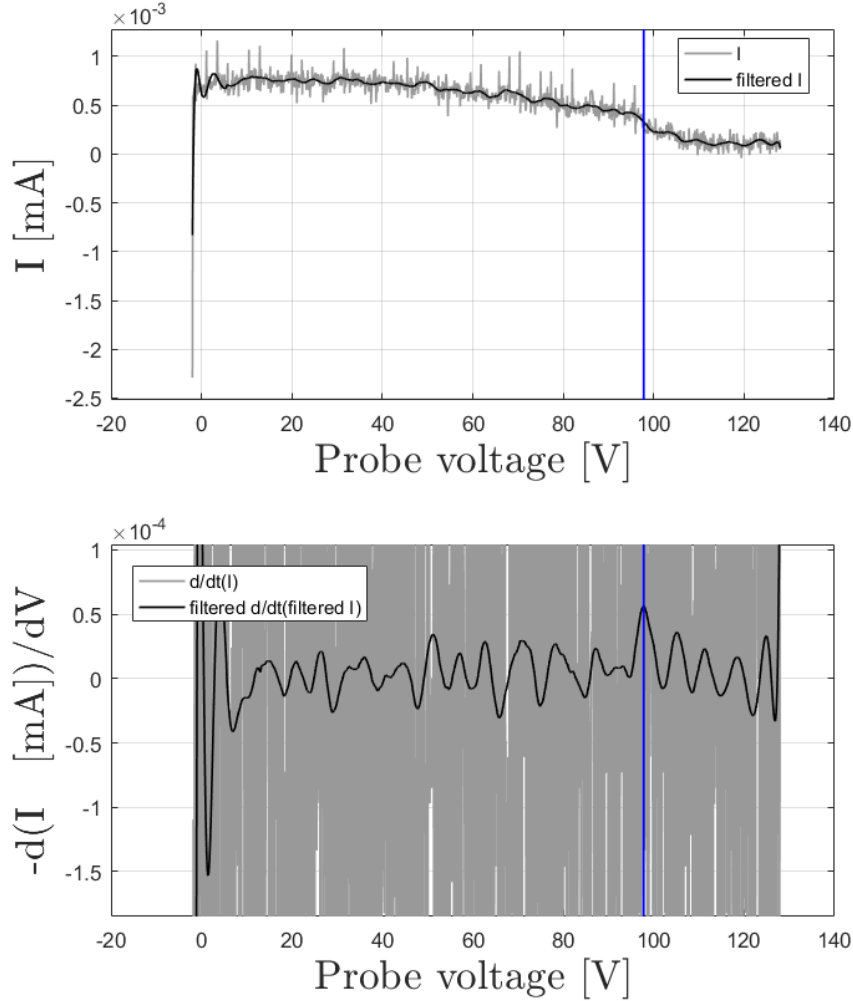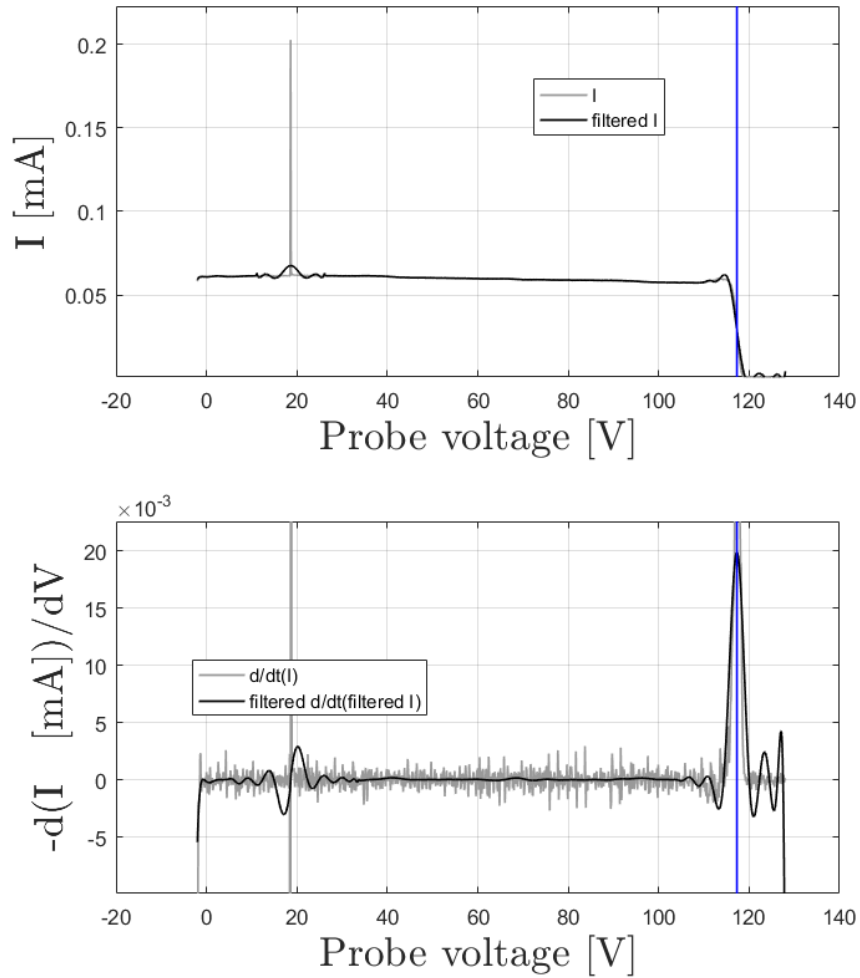
Figure 6.2: RFEA I-V curve obtained for the 1.5 sccm gas flow at the edge of the beam, 13 cm radial position. The blue line represents beam potential obtained from the derivative in the lower image. The probe voltage is the discriminator voltage -9 V to account for the negative bias on the collector as illustrated figure 4.10.

As can be seen from the derivative, the signal to noise ratio in figure 6.2 makes accurately determining the potentials difficult, but we use the highest peak as the presumptive beam potential in the I-V curves where we can

actually see the decrease in collected current with the increase in probe voltage. We ca take this as the beam potential because we know from the higher pressure results that the beam potential is in this region. We are however unable to see the plasma potential from the plots. Using this method to determine the beam potentials we get the radial profile of the beam potentials in figure 6.3.
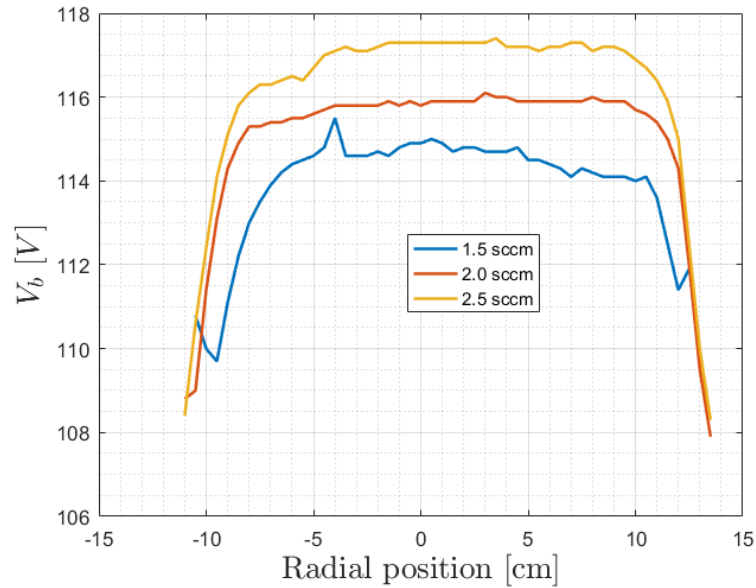
Figure 6.3:   Radial plot of the beam potential for the old configuration.

We see that the beam potential drops off at the edge of the beam, starting at 10-12 cm radial position on the positive side. At 14 cm the beam is no longer detectable for the 2.0 and 2.5 sccm gas flows, on the negative side the drop off seem to start at the -8-10 cm mark and by -11.5 cm beam is no longer detectable. For the 1.5 sccm regime the drop off starts sooner and the beam becomes undetectable closer to the grid.

Figure 6.4: RFEA I-V curve obtained for the 2.5 sccm gas flow at the center of the beam, 0 cm radial position. The blue line represents beam potential obtained from the derivative in the lower image. The probe voltage is the discriminator voltage -9 V to account for the negative bias on the collector as illustrated figure 4.10.

Further we have the issue that we in no way can determine the plasma potential from some I-V curves such as the ones in figures 6.2 and 6.4 due to the beam dominating the flux of ions to the probe. We can however see the plasma potentials in some of the I-V curves in the beam at higher pressures, but not all. To determine the plasma potential were the beam dominates we then have to look at the I-V curves obtained with the probe facing perpendicular to the beam, such as the one in figure 6.5. We can now determine the plasma potential in much the same way as we did for the beam potential. We determined that we had to use the perpendicular RFEA-measurements for the entire all radial positions 1.5 sccm gas flow as the beam dominates the signal completely when looking upstream.
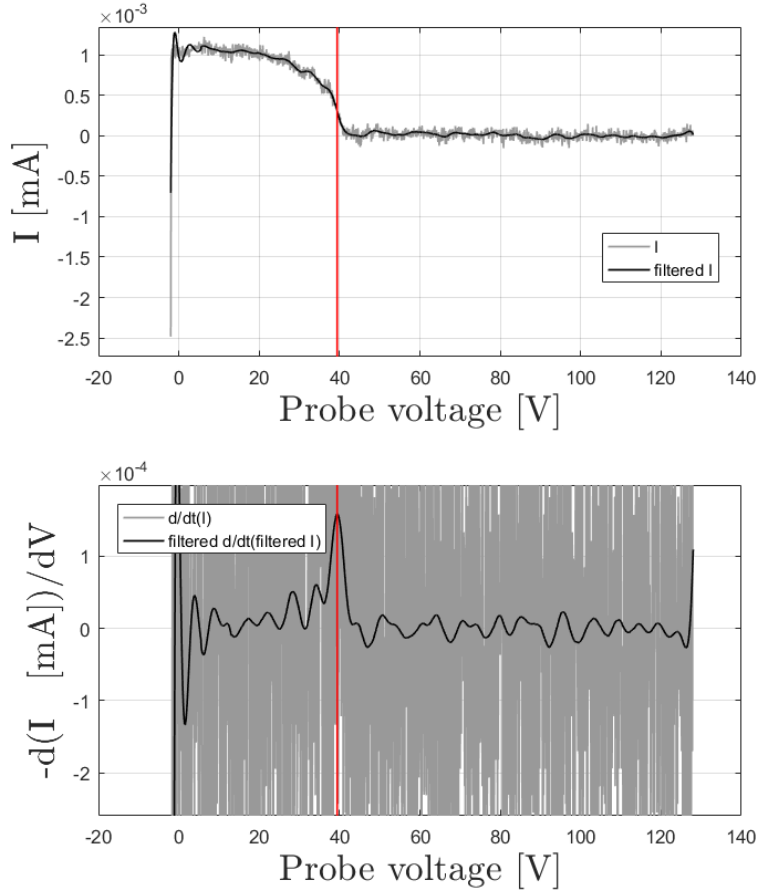
Figure 6.5: RFEA I-V curve obtained for the 1.5 sccm gas flow near the edge of the beam, 14 cm radial position perpendicular to the beam. The red line represents plasma potential obtained from the derivative.

For consistency we then used the perpendicular measurements for all gas flows and we obtained the plasma potentials seen in figure 6.6, although figure 6.7 shows that for the points where we can see the plasma potential with the probe facing upstream we get essentially the same values, but with far less consistency. Nonetheless we can see from the plots that the plasma potentials hover around 41.5 V for the 2.5 sccm gas flow, 42 V for 2.0 sccm and 42.5 V for the 1.5 sccm gas flow in the center of the beam. This fits with the expectations of higher plasma potentials at lower pressures [Lieberman

and Lichtenberg, 2005]

There is also a drop off at the edge of the beam present in all the radial plasma potential plots once you reach the beam edge, similar to the one in the beam potentials. This drop off is much more significant for the 1.5 sccm regime with a drop on the order of 5 V whilst the drops for the other regimes were more minute on the order of 0.5 V.
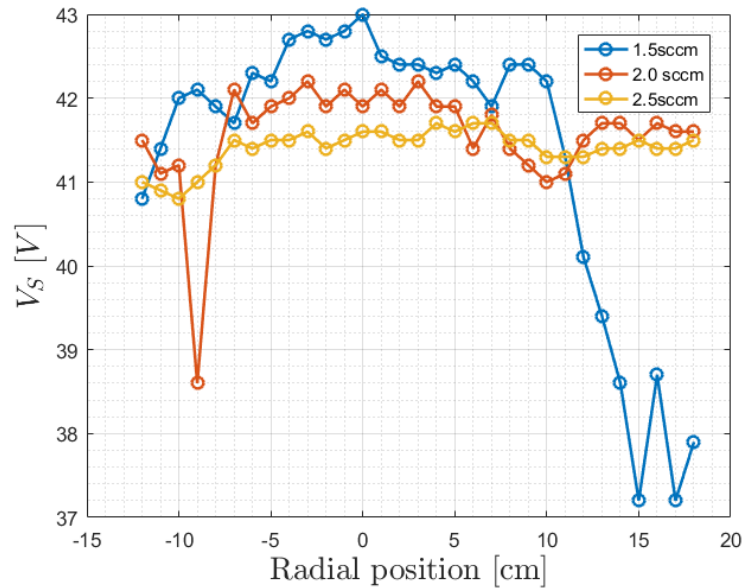
Figure 6.6: Radial plot of the plasma potentials obtained from the perpendicular plots.
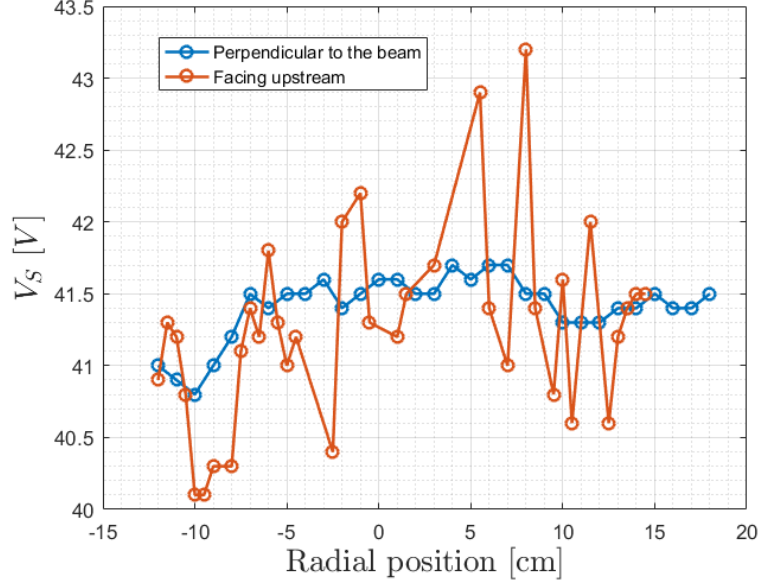
Figure 6.7: Radial plot comparing the detectable plasma potentials obtained from the I-V curves with the aperture of the probe facing into the beam to the ones obtained from the perpendicular plots at 2.5 sccm gas flow.

From the potentials we can now calculate the beam energy as in eV

$$E_b = e(V_b - V_S) \tag{6.1}$$

giving us the the radial energy profiles seen in figure 6.8. Where we see that the beam energy increases with increasing pressure due to the beam potential V_b rising with increasing pressure and the plasma potential V_S decreasing with increasing pressure. Figure 6.8 also shows the beam ion velocity.
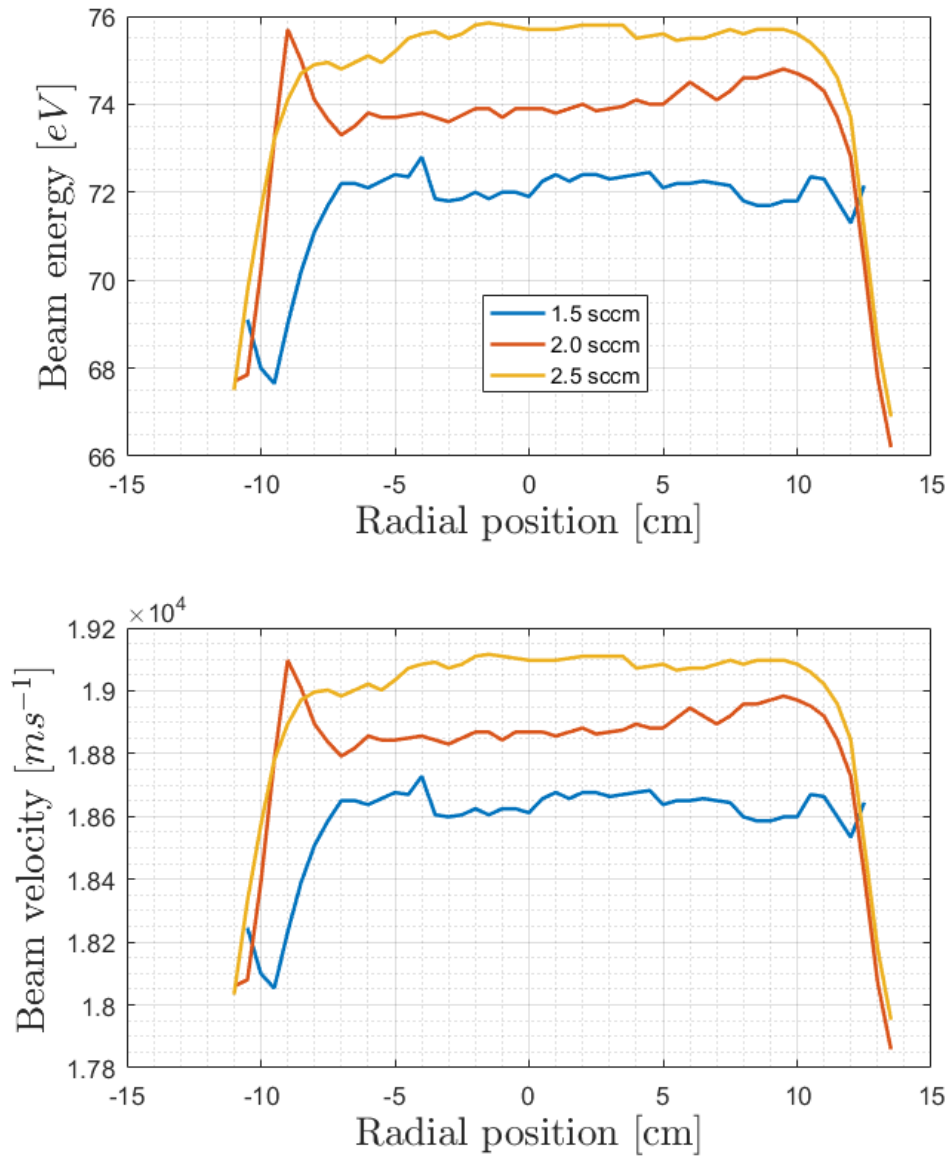
Figure 6.8: Radial plot of the beam energy in eV for all 3 gas flows.

The last variables that can be extracted from the I-V curves is the densities using the ion collection currents and equations 3.13 and 3.14. Using these equations leads to the results in figures 6.9 and 6.10.
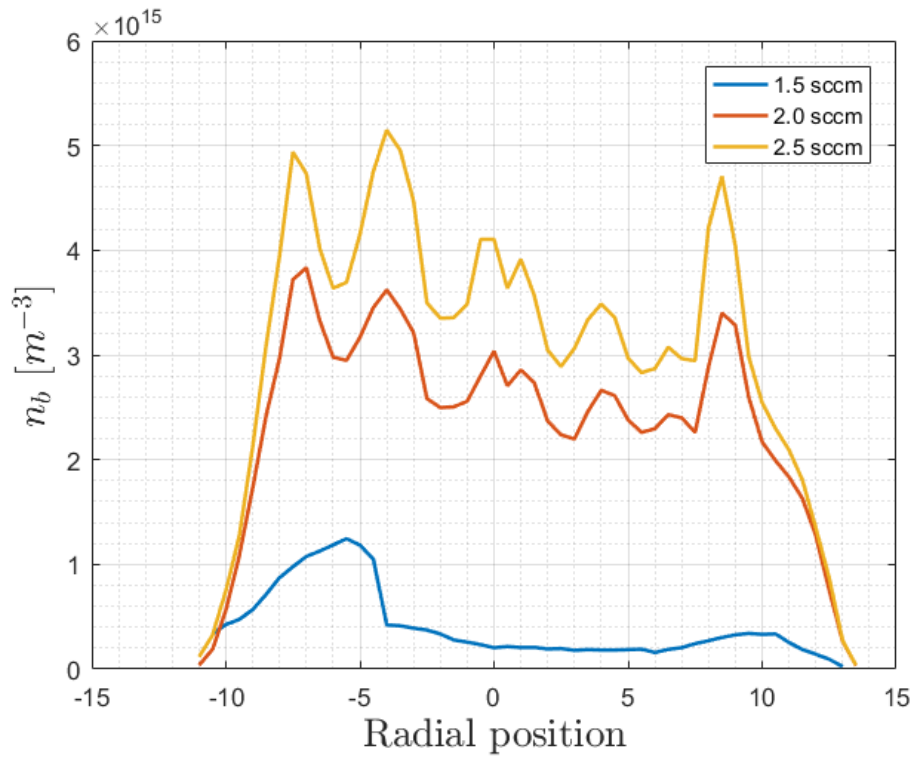
Figure 6.9: Radial plot of the beam density.
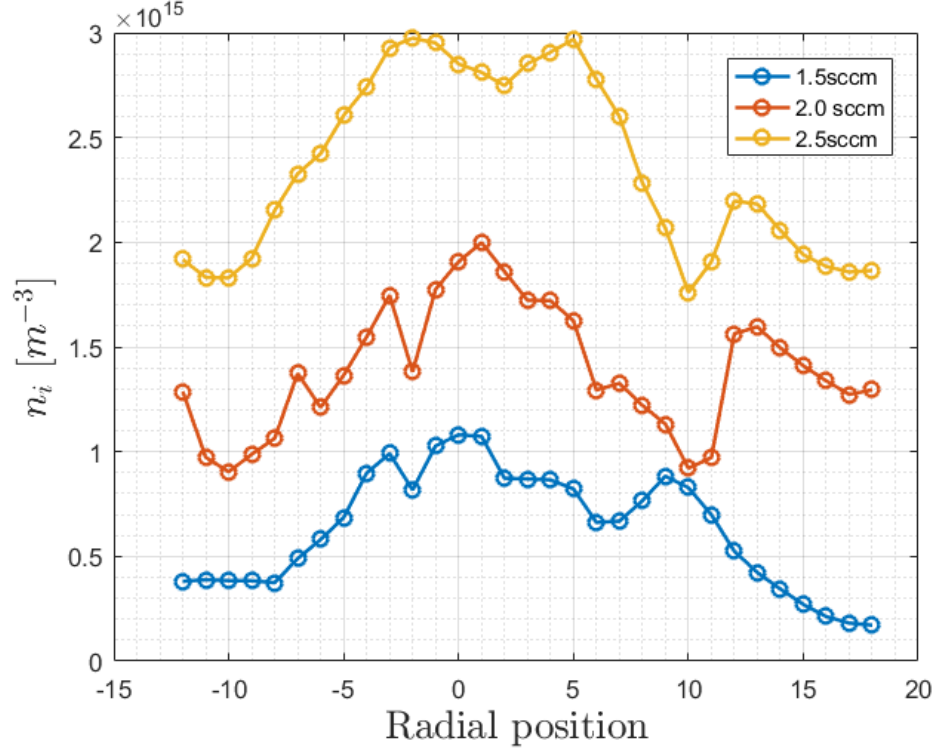
Figure 6.10:   Radial background density based on perpendicular facing
RFEA measurements.

As can be seen we have beam densities approaching $5 * 10^{15}$ m^{-3} at
the beam edges for the higher pressures and dropping slightly in the middle.
These increases in beam densities can also be seen on the density plot for the
1.5 sccm gas flow, but the densities at this pressure is much lower than the
higher pressures with $n_i = 10^{15}$ m^{-3}.

The background densities have a peak in the center of the beam at about
$n_i = 3 * 10^{15}$ m^{-3}, $2 * 10^{15}$ m^{-3} and 10^{15} m^{-3} for the 2.5 sccm, 2.0 sccm
and the 1.5 sccm gas flow respectively. The reason we most likely cannot see
the background plasma in the upstream measurements at the 1.5 sccm gas
flow is most likely due to the fact that the beam vel0city is much greater than
the ion acoustic velocity giving us a much greater flux from the beam when
compared to the one from the background plasma. We assumed an electron
temperature of $1eV$ for calculating c_S as this is consistent with previous

experiments done, [Osnes, 2016].

If we compare the plasma density gotten from the upstream facing source,figure 6.11, to the one in figure 6.10 we see that the magnitude of the currents match from the center of the beam and out in the positive radial direction, but there is a significant deviation on the far/negative side. Some asymmetry when the probe rods go through the beam has bees noted in earlier works [Gulbrandsen and Fredriksen, 2017]. Figure 6.12 shows the radial plot of the saturation current when facing upstream.
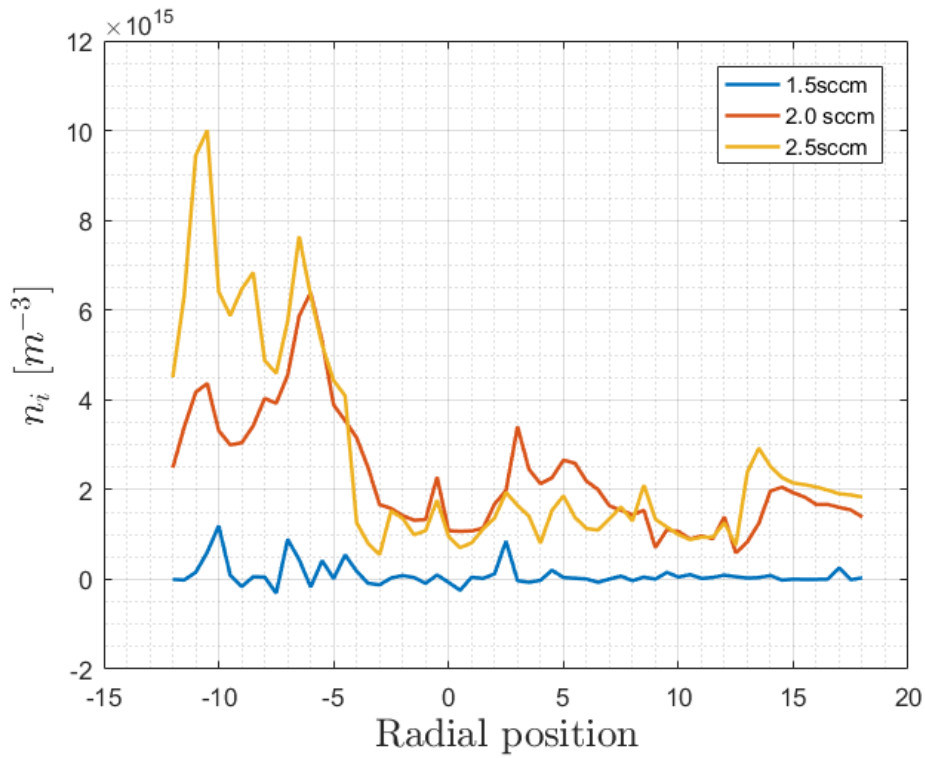
Figure 6.11: Radial plasma density plot based on the current in the saturation region with the beam current subtracted.
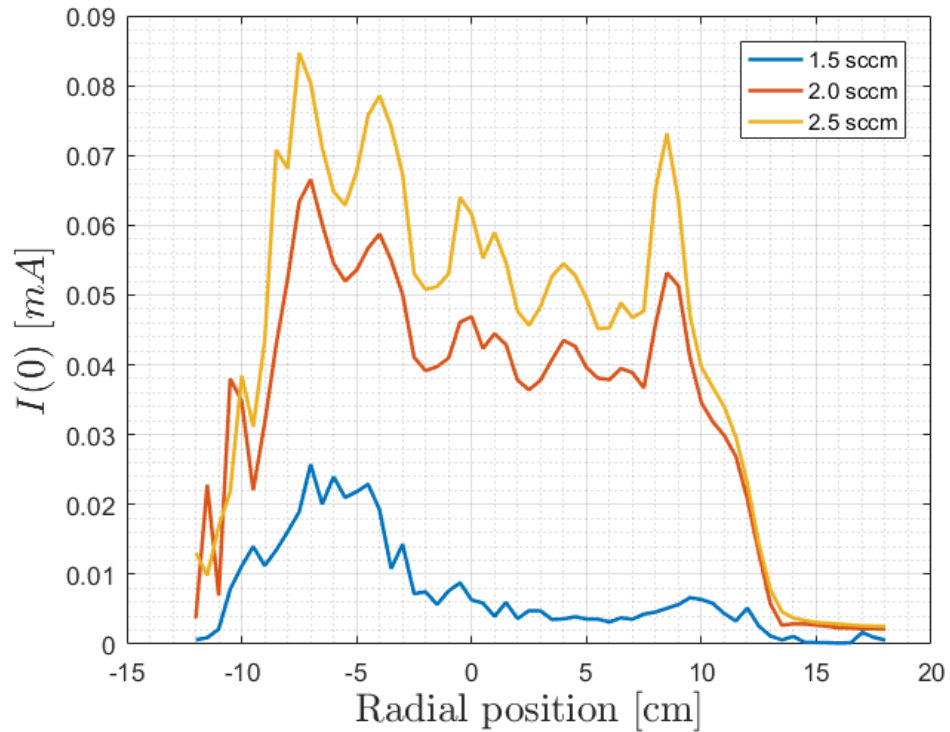
Figure 6.12: Radial total density plot based on the current in the saturation region.

6.1.2   New configuration

In the new configuration we find that the plasma potential and the beam potential is much more closely spaced as can be seen in figure 6.13.
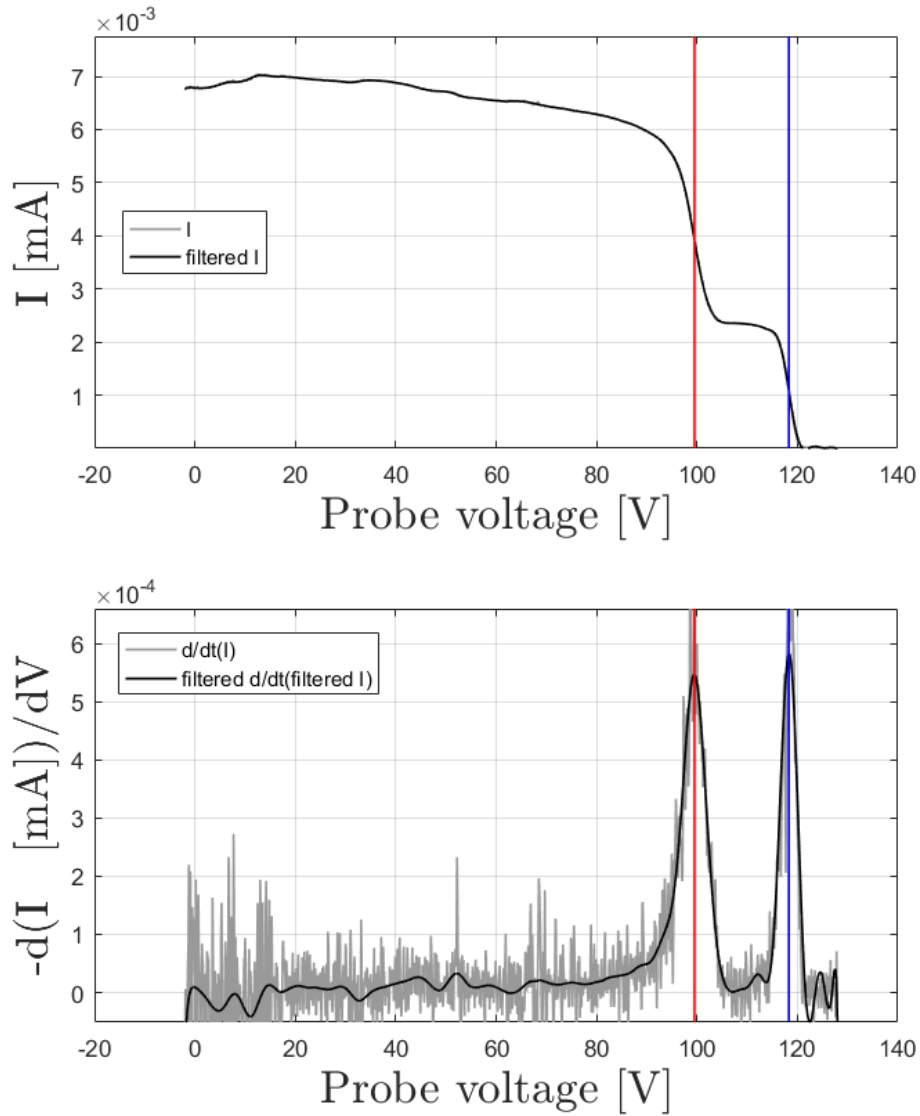
Figure 6.13: RFEA I-V curve obtained for the 2.5 sccm gas flow near the edge of the beam, 12 cm radial position in the new configuration.

A radial plot of these potentials can be seen in figure 6.14 and clearly shows that the beam potential remains near 120 V, but the plasma potential has been increased to about 104 V in the center of the beam.
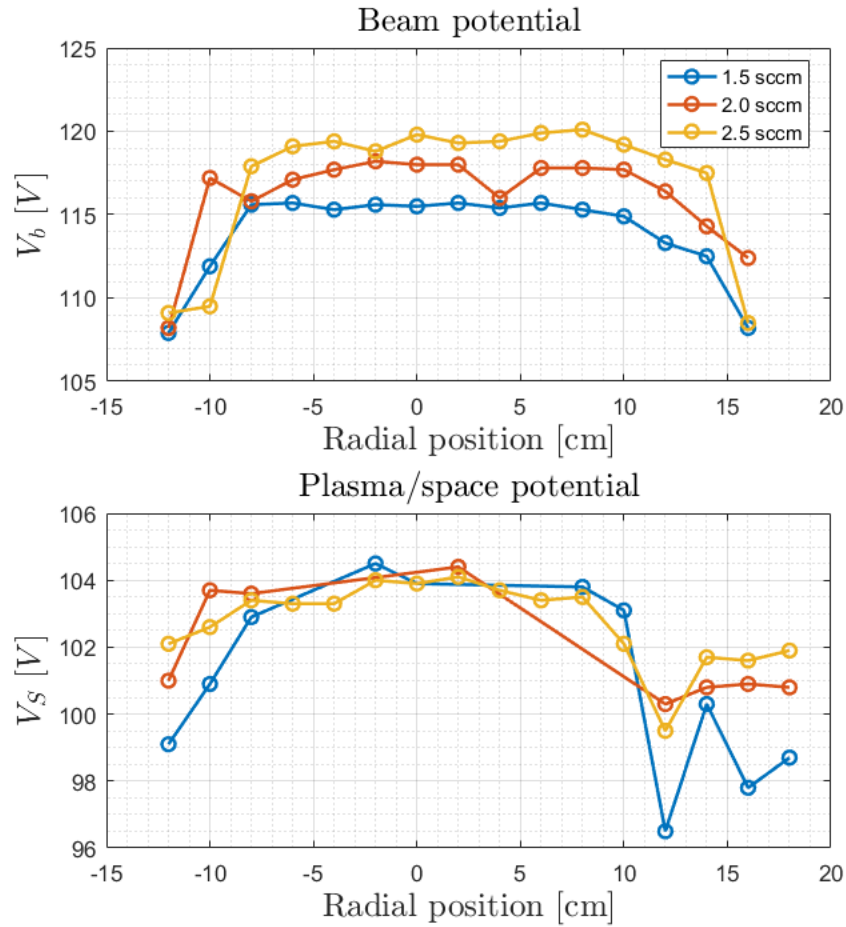
Figure 6.14:   Radial beam potential and background plasma potentials.

As a result of the increase in plasma potential has been reduced to 15-20 V for the 2.5 sccm in the center of the beam, down to 7 V at the edges. This becomes 12-16 V in the center of the beam for 2.0 sccm, down to 7 V at the edges and 11-17 V in the center of the beam for 1.5 sccm, down to 9 V at the edges. The beam energies and their corresponding velocities are presented in figure 6.15.
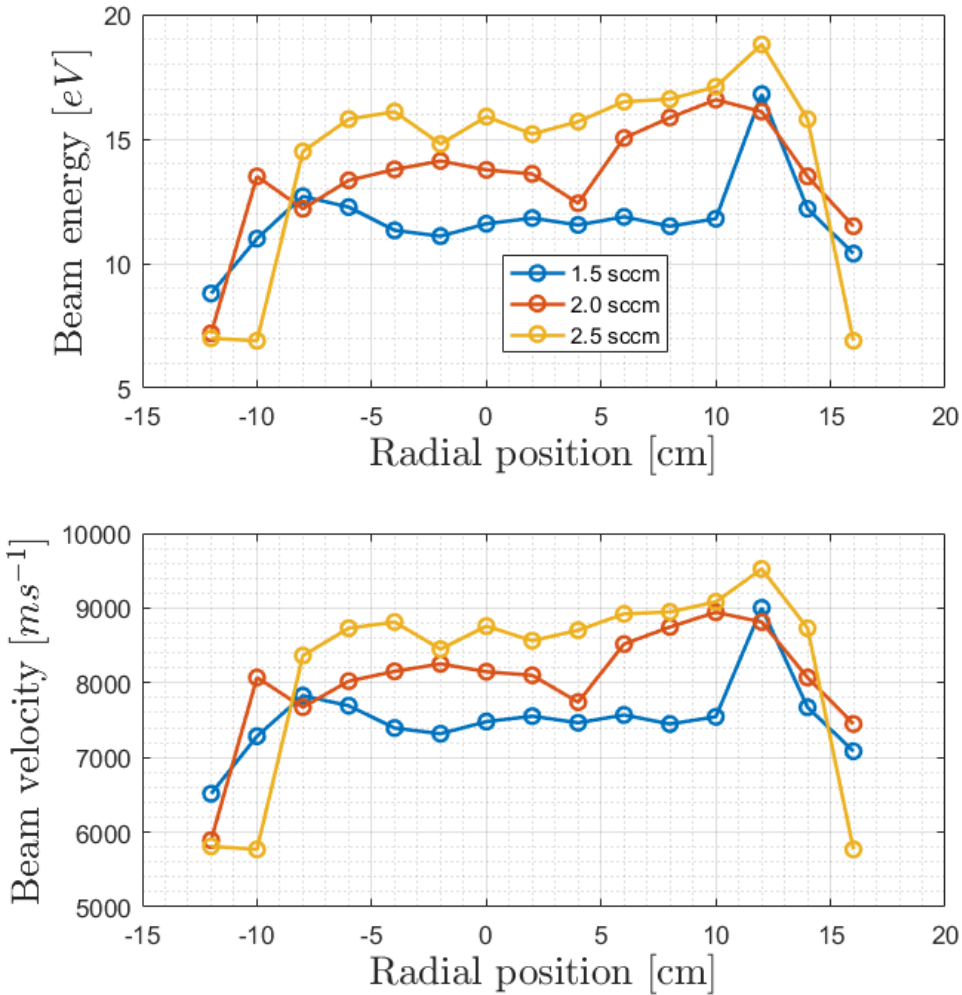
Figure 6.15: Radial beam potential and background plasma potentials.

As we were unable to acquire perpendicular measurements for the new configuration before the failure of the remaining filaments in the source we can only use the collection currents from the front facing measurements. This leads to the radial density profiles in figures 6.16 and 6.17. We used the electron temperatures of the 6 cm axial position of the Langmuir measurements to calculate the ion acoustic velocity soused in the density calculations.

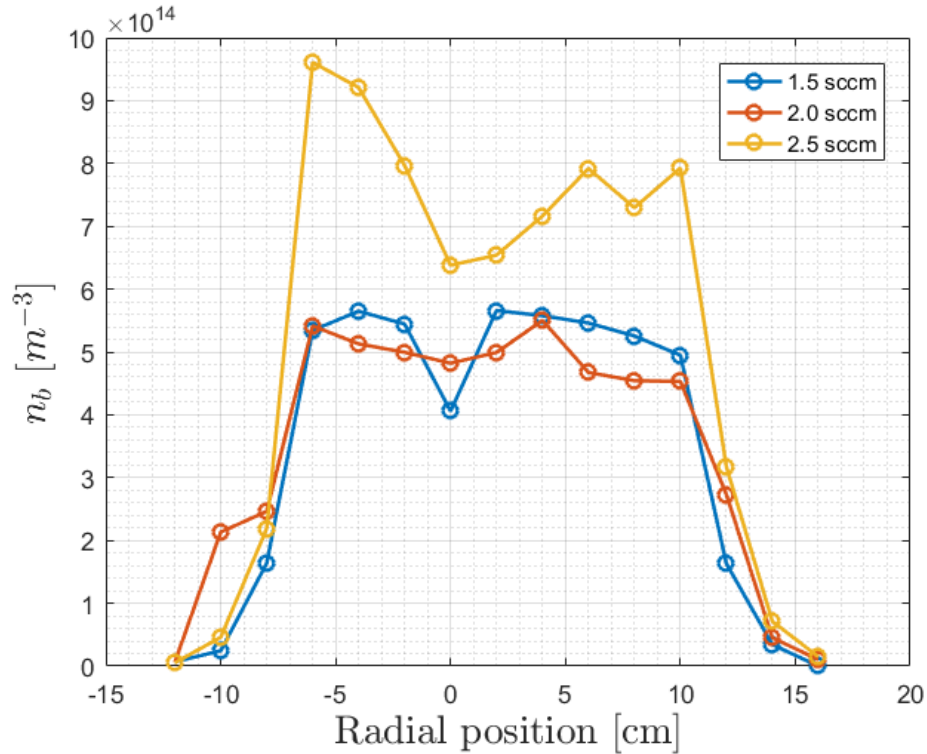As we saw from the comparison of the background plasma density mea-

Figure 6.16:   Radial plot of the beam density in the new configuration.

surements for the upstream facing source to the perpendicular source we will see a general indication of the plasma densities on the positive side of the radial profile. $n_i = 6 * 10^{15} m^{-3}$ for the 2.5 sccm flow as seen in the center of the profile. The lower pressures are only visible outside the beam, but we can draw some information out of it anyway. As the densities calculated show a rising trend towards the center of the distribution for the 2.5 sccm gas flow, with the other gas flows following at a shallower angle, we expect the densities to have a similar distribution to that seen for the old configuration. From the fact that the peak density calculated for the 2.5 sccm gas flow is approximately 2 times that of the old configuration we expect similar results for the other gas flows.

The saturation currents for the new configuration are seen in figure 6.18.
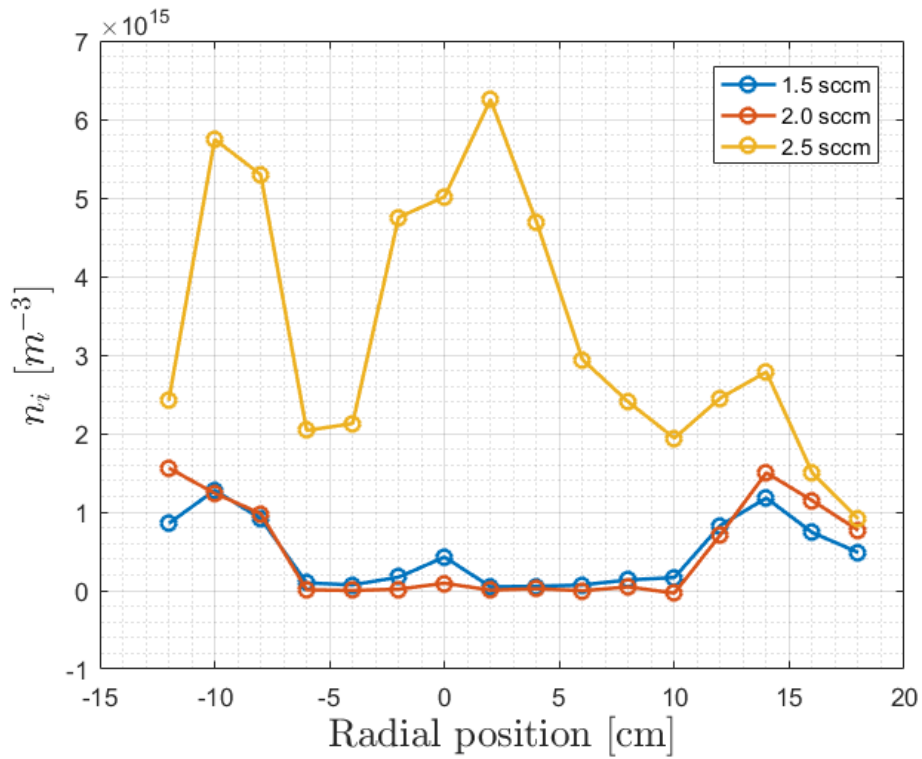
Figure 6.17: Radial plasma density plot based on the upstream facing RFEA measurements
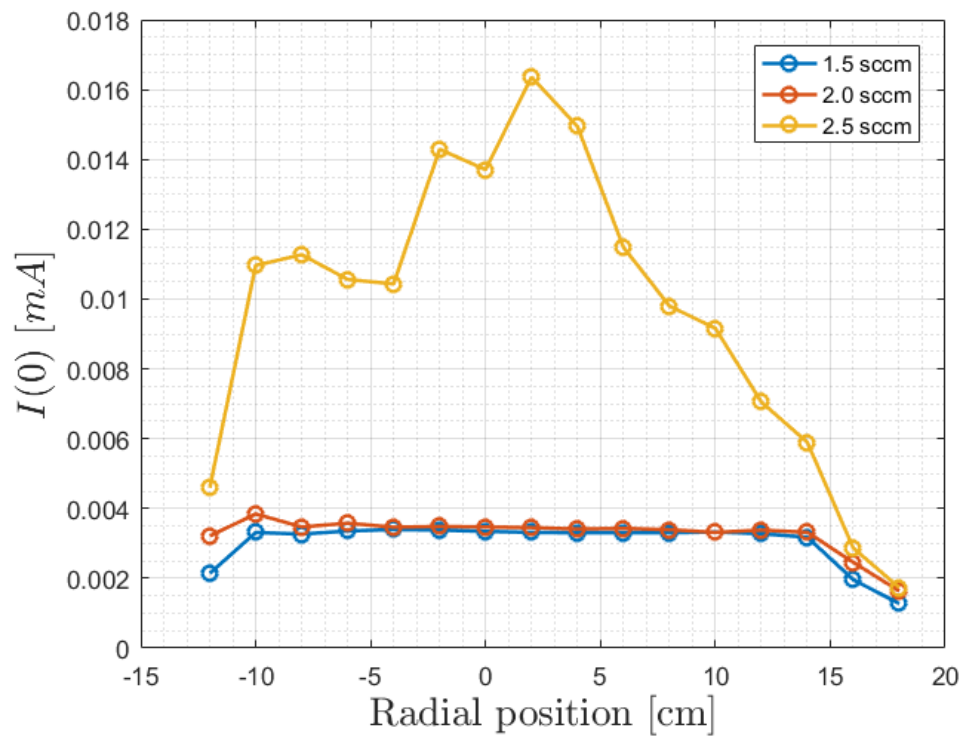
Figure 6.18: Radial saturation flux based on the upstream facing RFEA measurements

6.1.3 Configuration comparison

The effects that the change in configuration had can be seen when comparing the plasma parameters presented in the previous sections.

Figure 6.19 shows how the beam potential at the center of the beam is affected by the change in configuration. The effect is a slight increase in the beam potential, on the order of 1 V for the lowest pressure and 2.5 V for the highest. These increases, while not as drastic as some that will be described later in this section, also indicates that the new configuration is more sensitive to pressure as far as the beam potential is concerned, an increase in pressure causes a greater increase in beam potential compared to the old configuration.
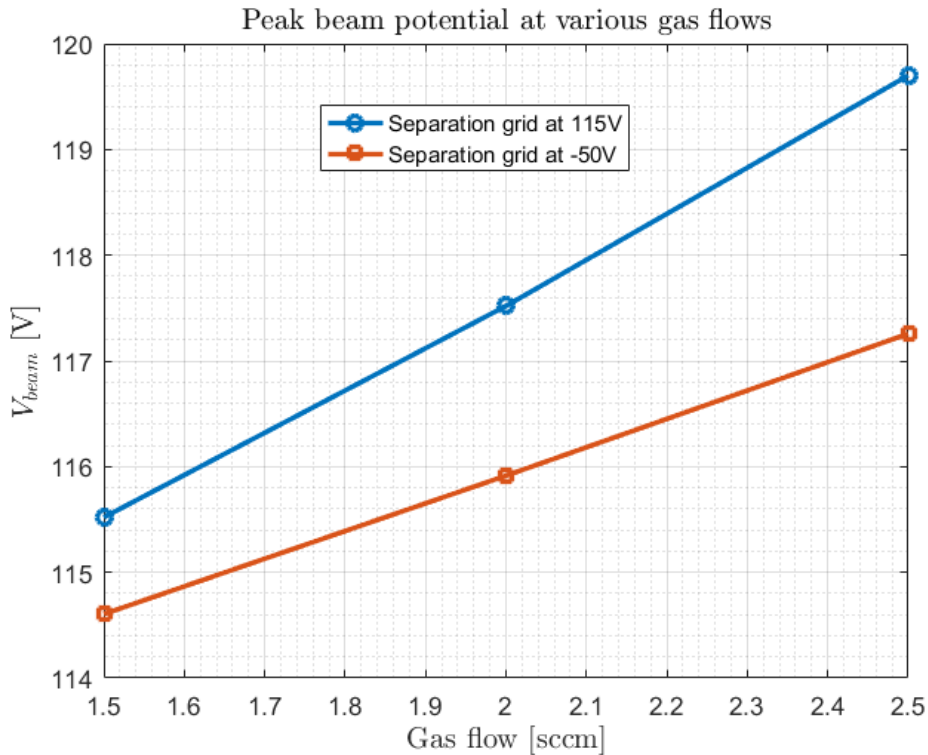

Figure 6.19: Comparison of beam potentials in the new and old configuration.

A far more significant effect is the increase in plasma potential we compare the background plasma potentials, figure 6.20. From the plot we can see

that the plasma potential has been increased by about 60 V in the new
configuration, to about 100 V, when we short-circuit the grid and the anode
cage. This then has the effect of greatly reducing the beam energy as as the
difference between the beam potential and the background plasma potential
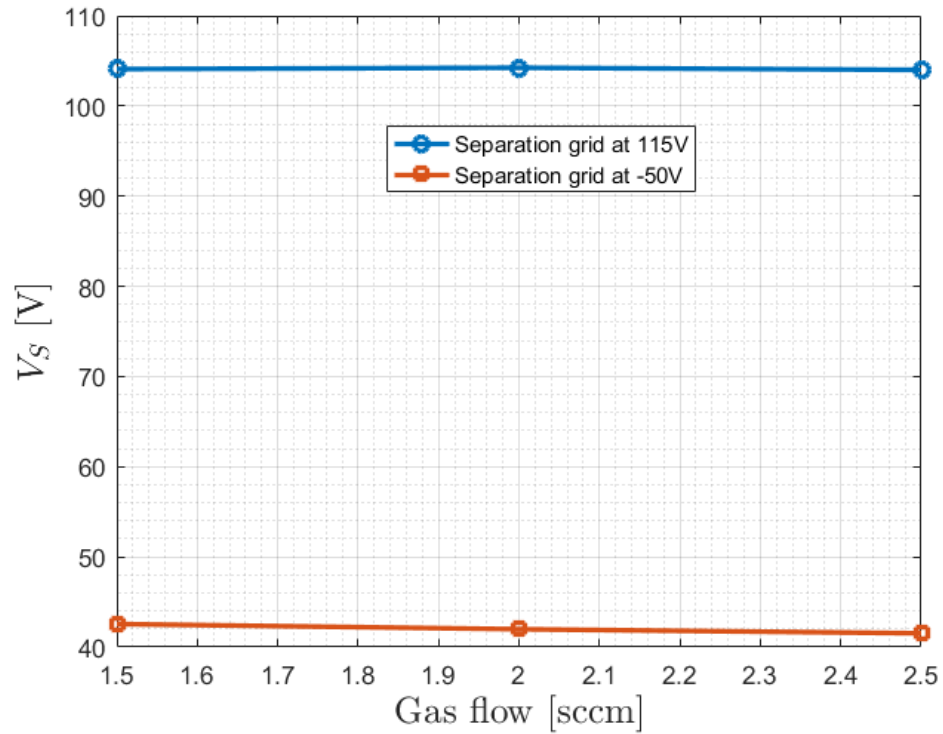is now 17-18 V as opposed to 72-76 V in the old configuration, figure 6.21.

Figure 6.20: Comparison of background plasma potentials in the new and
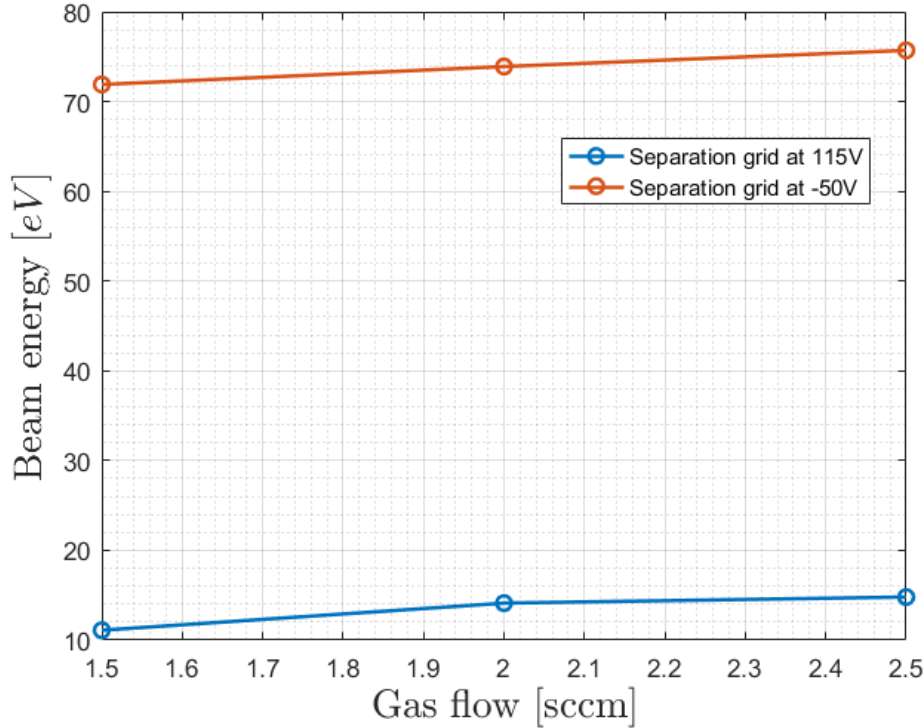old configurations, indicated by the separation grid potentials.

Figure 6.21: Comparison of beam energy for the different gas flows.

As we do not have comparable background plasma, perpendicular measurement, densities we will not directly compare the densities at the lower pressures, as we are unable to get a complete radial profile at these pressures. We do however see a significant increase at 2.5 sccm gas flow with a near doubling of the plasma density at this pressure, from $3 * 10^{15} m^{-3}$ at the center of the beam in the old configuration, to $6 * 10^{15} m^{-3}$ at the center of the beam in the new configuration.

As for the beam densities they had a reduction in magnitude to the order of 80% at the higher pressures, whilst only having the radial profile being smoothened out at the lowest pressure, 1.5 sccm gas flow. This equalized the beam densities for the 2.0 sccm and the 1.5 sccm gas flows.

If we compare the saturation to the probes in figures 6.12 and 6.18 we see that the new configuration increased the total flux of ions to the probe at 1.5 sccm and 2.5 sccm, whilst not changing the flux to the probe at 2.0

sccm to any noteworthy degree. This is the cause for the changes in beam densities and plasma densities.

6.2   Langmuir results

This section will cover the data collected by the Langmuir probes. The section is divided into 2 subsections where one will go over the results gathered for the radial positions with a 6 cm axial position in order to highlight radial effects and the other section will focus on the axial development of the parameters presented for the 6 cm axial position.

6.2.1   I-V curve measurements at 6 cm axial distance

Figure 6.22 shows how the raw I-V curves looked for our experiments. As can be seen from the units the magnitude of the collected currents especially on the electron side of the plot is increasing with pressure indicating a higher plasma density. Further we see that the center curve, 0 cm radial position, draws the largest current and as such we expect to have the highest density here, with the density trailing off towards the edges, as seen in figure 6.23.
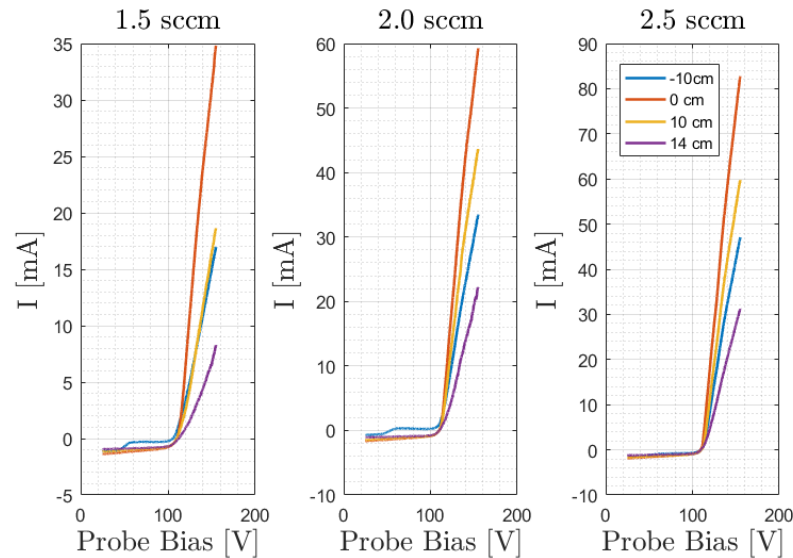

Figure 6.22:   The I-V curves for the various radial positions with a 6 cm axial position for all pressure regimes.
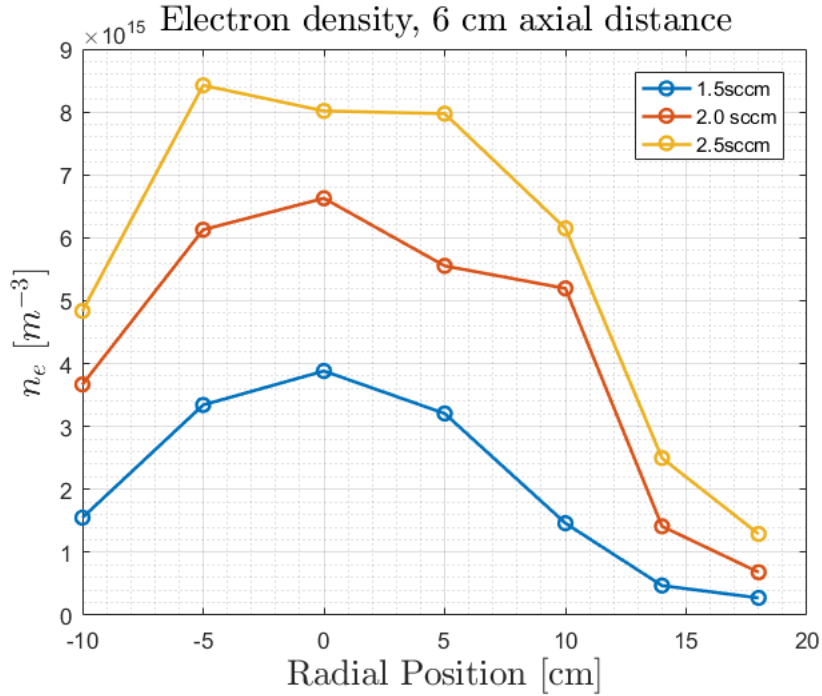
Figure 6.23: Radial plot of the electron densities at the various gas flows

The densities were calculated using the electron current at the plasma potential using equation 3.5, with the temperatures, such as in figure 6.24, and plasma potentials, figure 6.25, obtained using the classical method described in section 3.1, i.e. the linear fit to the logarithmic curve and their intersection. This leads us to obtain electron densities that peak at on the order of $n_e = 9.5 * 10^{15}$ m^{-3} at the center of the aperture for the 2.5 sccm gas flow. This is reduced to about $6.5 * 10^{15}$ m^{-3} and $4.0 * 10^{15}$ m^{-3} in the 2.0 and 1.5 sccm gas flows respectively.
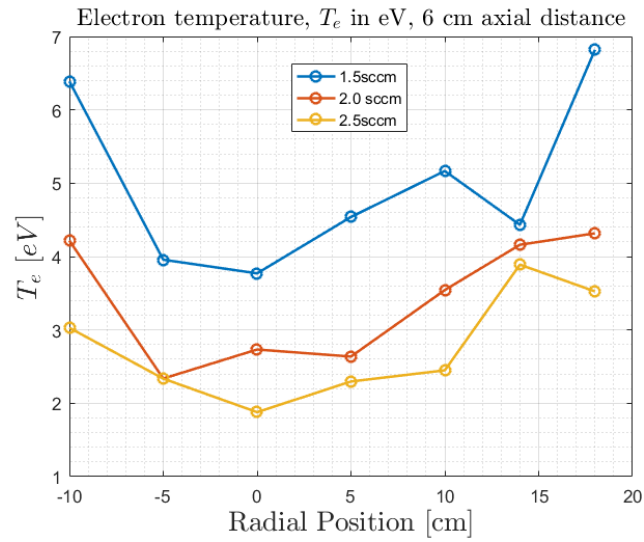
Figure 6.24:   Radial plot of the electron Temperatures in eV at the various pressure regimes using an axial distance of 6 cm.
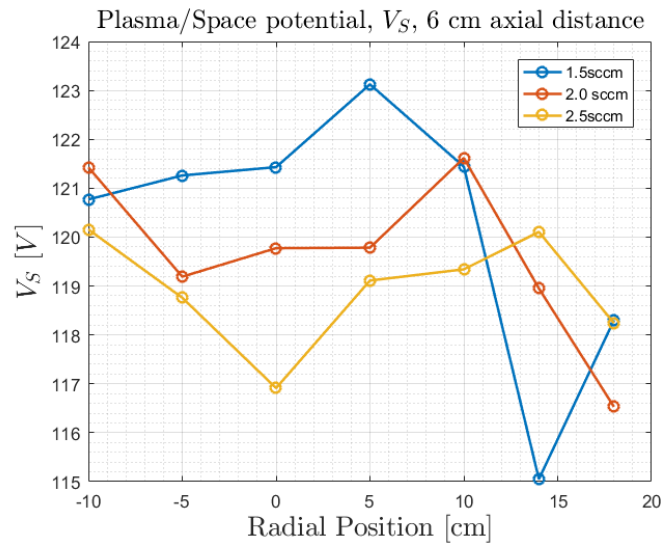

Figure 6.25:   Radial plot of the plasma potentials.

If we look closely on the I-V curves for 1.5 sccm and 2.0 sccm we can see that the -10 cm I-V curve has and abnormal increase in the region 40 V to 60 V indicating the presence of a electron beam. This increase is also present at 2.5 sccm, as can be seen in figure 6.26, although the change is far less visible than for the other pressures in part due to the increased strength of the normal I-V curve signal.The locations of these increases in the collected currents can also be seen in the derivative of the current, figure 6.27.
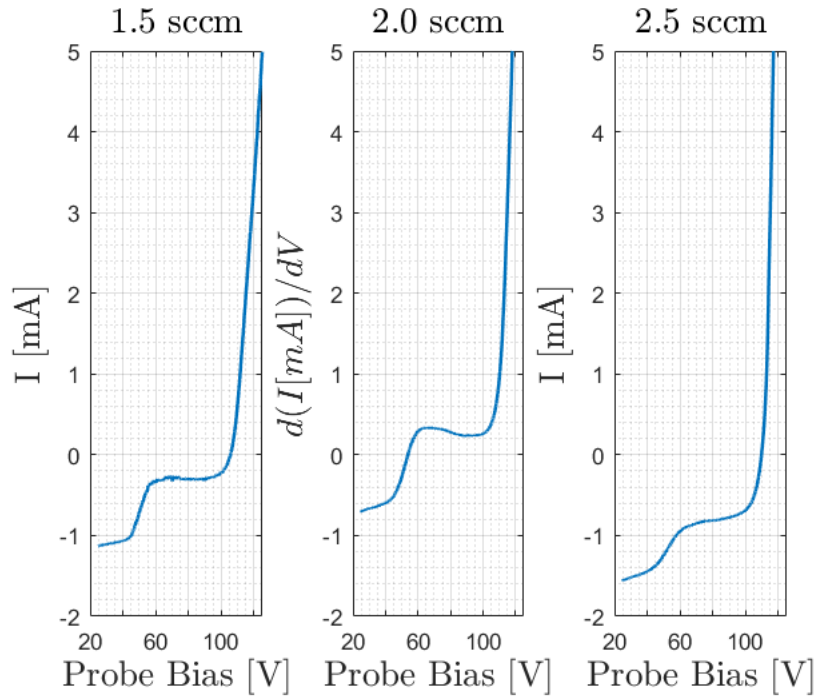

Figure 6.26: The I-V curves at the -10 cm radial position with a 6 cm axial position for all pressure regimes.
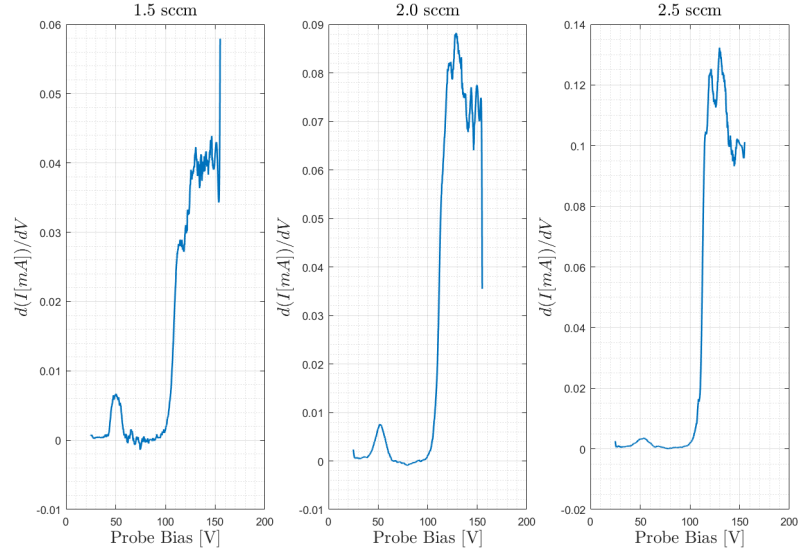
Figure 6.27:   The derivative of the I-V curves at the -10 cm radial position
              with a 6 cm axial position for all pressure regimes.

The derivative shows that the beam is centered around 50V, giving us beam energies on the order of 70 eV. The beam energies will be presented in the latter part of section 6.2.2.

6.2.2   Axial development of plasma parameters

As we repeated all our measurements every 6 cm in the axial direction we can now see how the plasma parameters evolve with increasing axial distance.

The first variable we can look at is the plasma potential, figure 6.28. The trend as seen from the color plot appears to be a region of higher plasma potentials outside of the edge of the aperture, 10 cm radial distance, that peaks at about 18 cm radial distance. This region also appears to become smaller as the pressure increases indicating the the high potential areas are related to a lower of plasma density. From the increase in the plasma potential seen at the 18 cm axial position at 1.5 sccm gas flow we can be reasonably sure that we have some shadowing effects, as the decreased density leads to a shallower slope in the I-V curve, resulting in higher calculated temperature and plasma potentials.
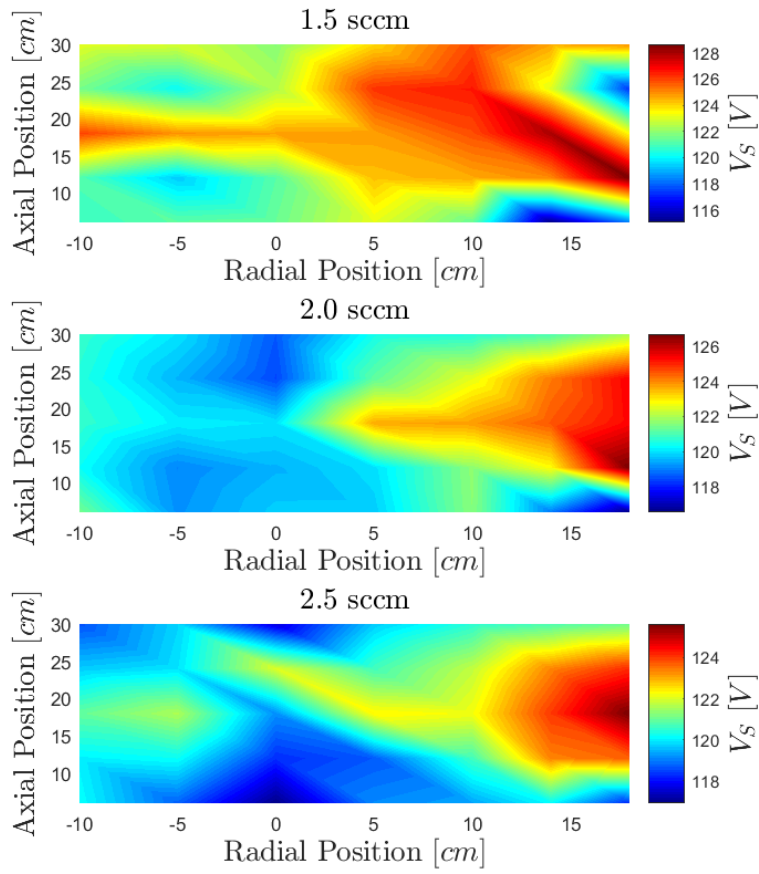
Figure 6.28:   Plasma potential distribution at all 3 gas flows.

The plasma potentials we see there might in part be explained by the fact that we have higher electron temperatures in those regions, figure 6.29, and lower densities, figure 6.30.
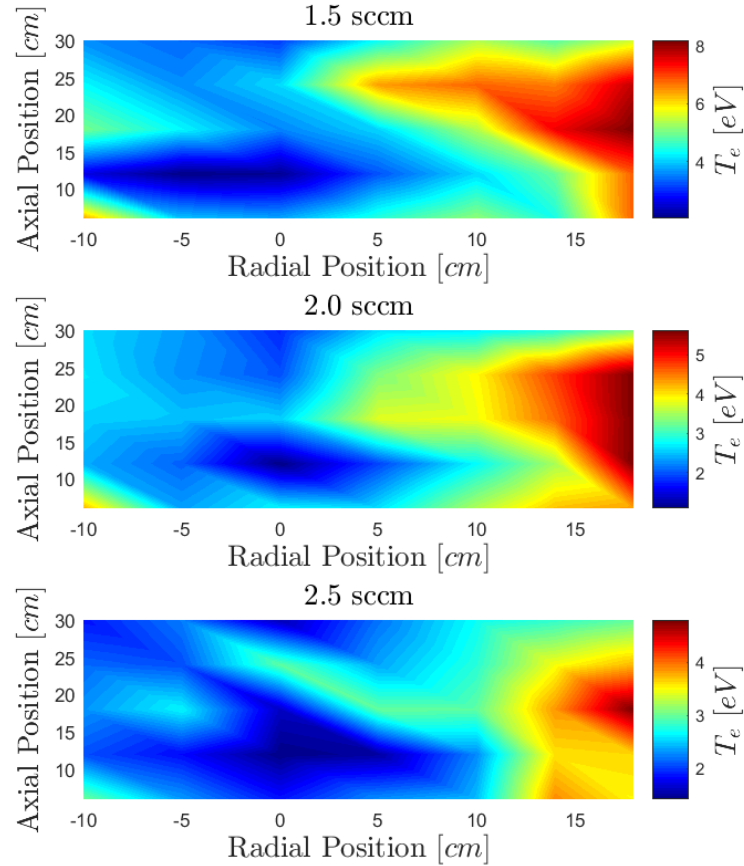
Figure 6.29: Electron Temperatures in eV for all 3 gas flows.

The densities obtained using equation 3.5 are presented in figure 6.30. As can be seen by comparing these color plots we see that the general electron density is increasing with pressure as was the case at 6 cm axial position, figure 6.23.

The 18 cm and the 24 cm axial positions show a distinct decrease in density that is present in all gas flows. Given that they were taken using a

probe that further back from the separation grid, i.e they had other probes ahead of them when looking upstream we can assume that there was some shadowing for this particular probe.

Given that we have seen from the RFEA measurements that the plasma is largely dominated by a beam we can assume that the possible shadowing would have a drastic effect on the collected plasma. Due to this we have elected to compare the electron densities to the density at the 0 cm radial position along the same axial distance, figure 6.31.
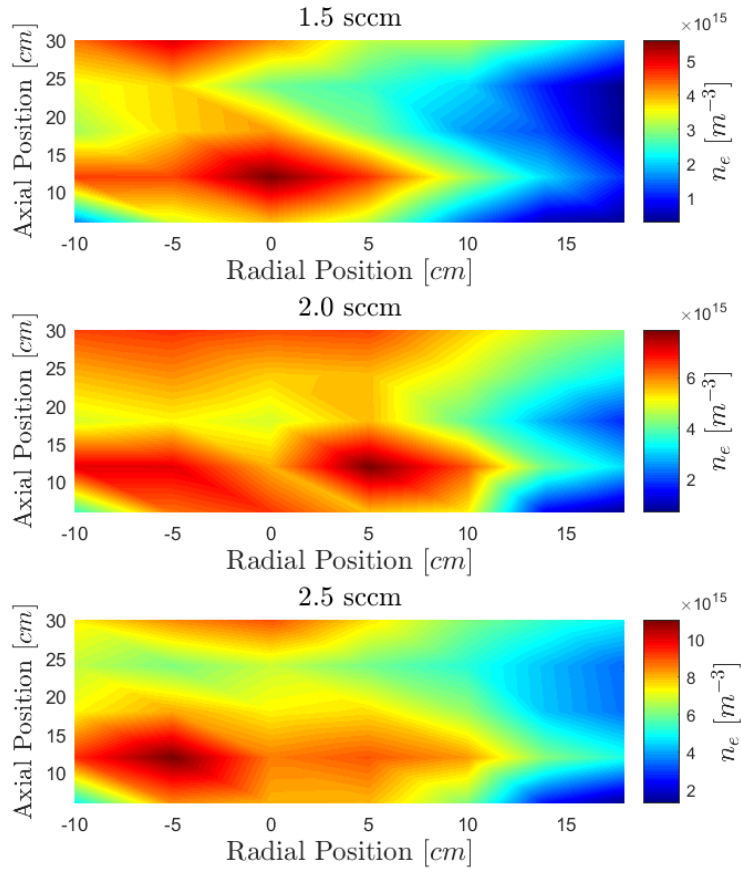

Figure 6.30: Electron density distribution in the measurement plane for all 3 gas flows.
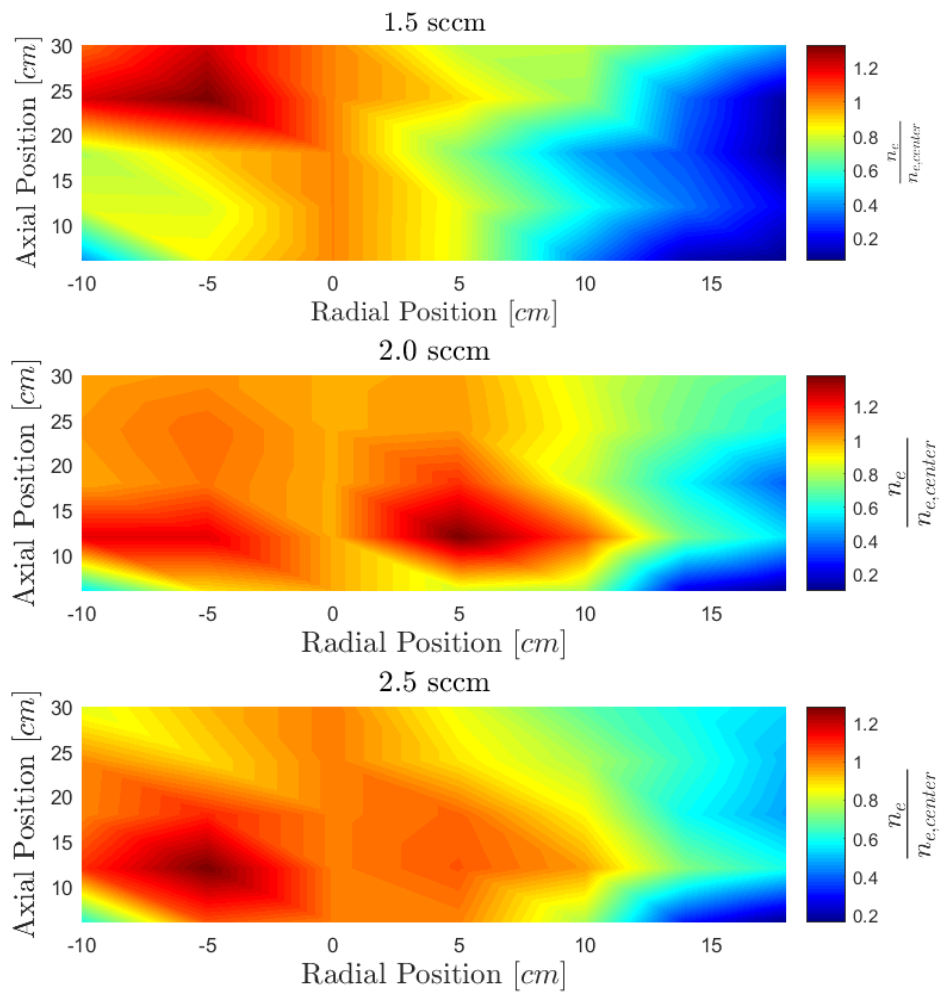
Figure 6.31: Electron density distribution in the measurement plane for all 3 gas flows normalized against the densities at the 0 cm radial positions.

From the distributions in figure 6.31 we see that the distributions drop off at a greater rate radially the closer you are to the source of the plasma and the lower the pressure, indicating diffusion which is what we would expect, grater diffusion the further you are from the source and the greater the pressure.

The last parameter we have to consider an axial development for is the presence of the electron beam observed at the -10 cm radial positions in section 6.2.1. Although we could see the evidence of the high energy electrons, steepening of the slope of the I-V curve in the ion saturation region of the i-V curve, in other radial positions we have only included the ones that had a distinct maxima in the derivative, thus enabling us to calculate the beam energy. These were found at the far edge of the grid, i.e. at the -10 cm radial position.

As it is the voltage of the probe relative to the plasma potential that determines the minimum energy an electron or ion must have in order to be collected by the probe, we can plot the potential of the derivative peak with respect to the plasma potential to obtain the beam energy, same as with ion beams.

We find that the potential differences increases as the pressure decreases. The peak potential difference increases from in the "electron beam" with respects to the background plasma as obtained by the Langmuir probes is 68 V for the 2.5 sccm gas flow, 69 V for the 2.0 sccm gas flow and 73 V for the 1.5 sccm gas flow.
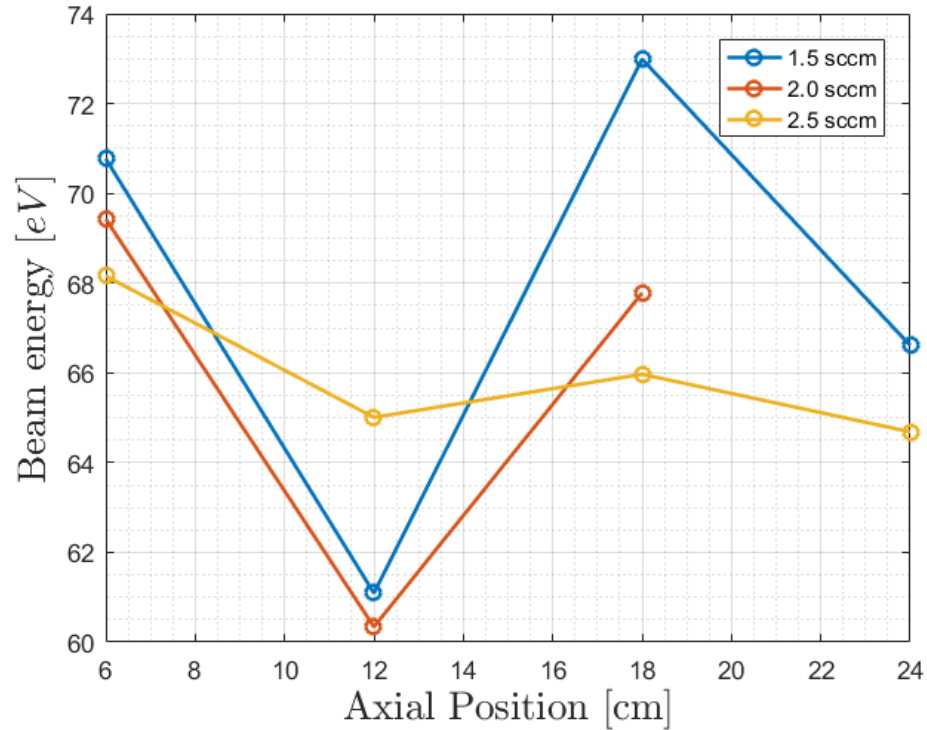
Figure 6.32:   The beam energy of the electron beams at the -10 cm radial position.

The final parameter that we looked at is the magnitude of the electrostatic fluctuations measured with the Langmuir probes and the oscilloscope. These measurements are presented in figure 6.33 and show that the magnitude of the fluctuations, represented by the standard deviation of the signal σ, is fairly uniform. We do however see some spikes in the turbulence on the far side. This is the case for all 3 pressures.

Figure 6.33: The magnitude of the fluctuations at all 3 pressures.

Chapter 7

Discussion

This chapter aims to compare the results gathered from all the experiments and to possibly provide a physical explanation for the phenomena uncovered.

7.1 The effect on ion beam parameters

From section 6.1.3 we see that the beam potential as measured by the RFEA probe is largely unchanged, at least compared to the change we observe in the plasma potential measured by the RFEA-probem which is drastically increased in the new configuration.

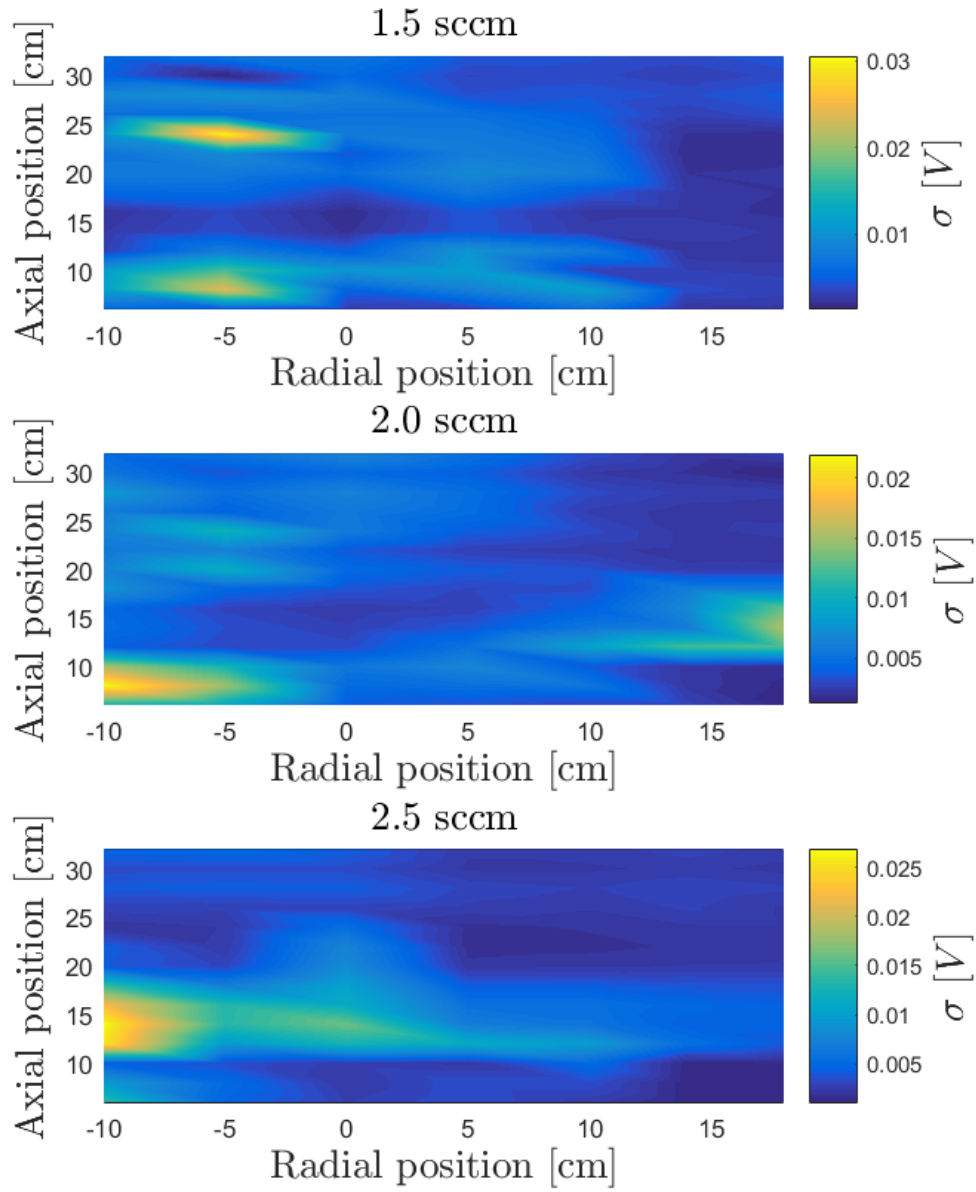This increase might be because the plasma in the source now sees the separation grid as a chamber wall leading to a sheath drop of $V_{sheath} \approx 4.7Te$ [Lieberman and Lichtenberg, 2005]. From the beam energies seen in the new configuration this would indicate a temperature of 3.3 eV, 3.1 eV and 2.5 eV for the 1.5 sccm, 2.0 sccm and 2.5 sccm gas flows respectively. This is generally consistent with the temperatures measured, with the temperatures in the 0 cm radial position being within $\pm 20\%$ of this value.

It is not just the plasma potentials measured that changed however, the densities also changed quite a bit. We experienced a drastic fall in beam densities for the 2.5 sccm and the 2.0 sccm gas flows. The decrease was to the tune of 80% from $n_b \approx 5 * 10^{15}$ in the old configuration to about $n_b \approx 10^{15}$ in the new configuration. This is likely the result of the fact that in the old configuration, the negative grid potential represented a far larger drop in potential, and as such the ions were more attracted to the grid.

The reduction in beam energy accompanied by the reduction in beam

density leads to the conclusion that the old configuration with the negatively biased grid is far superior to the new configuration in terms of producing a dense, more powerful beam of ions.

7.2   Background plasma

When it comes to the Langmuir measurements, we see from the radial density profile at the 6 cm axial distance exceeded the plasma density calculated from the RFEA probe by about 50%. The overall shape matches what we observed from the 2.5 sccm radial density plot in the new configuration, apart from the increase at the far edge of the beam. This might in part be due to the fact that the RFEA probe is inserted along the same axial position and is crossing the beam when we reach the negative radial positions, similar to Gulbrandsen and Fredriksen [2017]. Accounting for the the 50% increase in the Langmuir measurements, we now have further evidence of the background plasma density increasing, by a factor of 2 for all pressures.

We also saw that the radial plasma potentials measured by the Langmuir closely matched the beam potentials at the 6 cm axial position. The reason for this is most likely the increase in the magnitude of the grid voltage in combination with the low density skewing the potential slightly higher. Osnes [2016] found for negative grid biases, a variation of the old configuration, that as the magnitude of the negative grid potential increased so did measured plasma potential from the Langmuir probe, figure 7.1, at the 0 cm radial position further downstream than the positions measured in our project. The increase in plasma potential is also evidenced in Hollenstein et al. [1980]. We now postulate that the effect might be dependent on the magnitude of the grid voltage.

A contributing factor that probably aided in shifting the measured RFEA beam potentials closer to the measured Langmuir plasma potentials is the fact that the RFEA can show potentials up to 5V lower than the actual potentials, in effect shifting the potentials, [Gulbrandsen et al., 2013].

Hershkowitz [2005] also states that the planar Langmuir probe will deviate from the true plasma potentials in the sheath region of a double layer. This means that the plasma potential measured by the Langmuir probe in our experiment might be false in the region close to the grid.

When looking at the axial development of we find that once we are outside the beam, the decrease in density and increase in temperature drives the
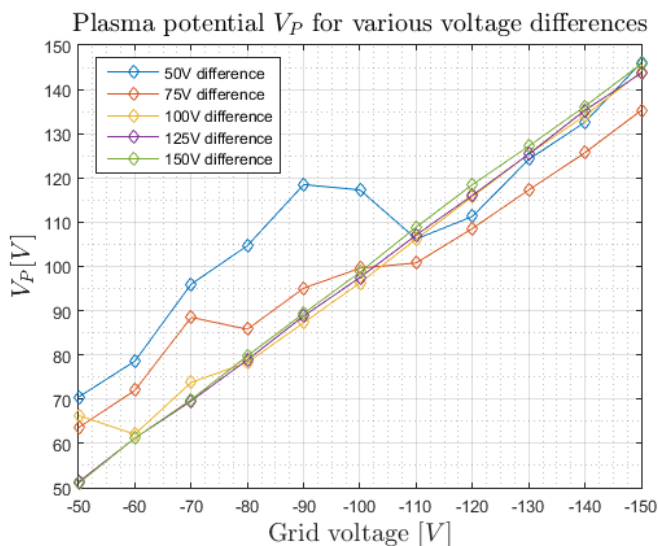
Figure 7.1: "Plot of plasma potential as a function of grid voltage" Plot from figure 27 in [Osnes, 2016](Plasma potential is in this plot V_P instead of V_S as it has been for the other parts of the paper)

measured plasma potential up. This was the case for all axial positions, however the shadowing effect on some of the probe tips makes a direct axial comparison of the plasma parameters not viable. The shadowing leads to an increased temperature measurement, decreased density and increased plasma potentials, as can be seen from the 18 cm and 24 cm axial positions on the plots in section 6.2.2.

As explained in section 6.2.1 the -10 cm radial position in the new configuration shows evidence of an electron beam, with the axial beam energies being plotted in figure 6.32. The beam energies seem to be increasing with the decreasing pressure, and subsequent increase in the mean free path.

From the peak beam energies detected we postulate that as the pressure decreases the beam energy approaches the anode-cathode potential difference in the new configuration, which is in line with what we can expect given that the grid is biased at the anode potential. This leads us to postulate that given a grid bias equal to the anode potential one might be able to diagnose how effective discharge current is at ionizing the neutral gas in the source, from outside the source by looking at the electron beam energy. The beam density might also be an indicator, but that is left for future research where

one can use a probe that is not being blocked by anything, i.e. no shadowing.

Finally we saw that the magnitude of the electrostatic fluctuations downstream from the source is fairly uniform with some spikes in the fluctuations on the far side of the separation grid. Due to the shadowing effect on the probe we cannot conclude anything from the fluctuation measurements, but the consistency in terms of the location of the spikes in fluctuations indicate that there is a greater turbulent plasma flow on the far side of the grid.

From the RFEA measurements in the old configuration we saw higher beam densities at the edge of the grid on the far side at all pressure. This along with the fact that we found the electron beams as the fluctuation spikes on that side indicates an unevenness in the source. Which makes sense given that we knew prior to commencing the experiment that some filaments had failed.

Chapter 8

Concluding remarks

We have performed analysis of the downstream plasma in the Njord double-plasma device at UiT when we only produce filament plasma in the source. We performed our experiments for two potentials of the grid separating the source and target chamber, -50 V and 115 V which was the anode potential. The experiments were repeated for pressures of $2 * 10^{-4}$ mbar, $5 * 10^{-4}$ mbar and $9 * 10^{-4}$ mbar, corresponding to the gas flows of 1.5, 2.0 and 2.5 sccm of argon.

We found from RFEA and Langmuir measurements that when we go from a strong negative bias to the anode voltage the induced plasma in the target chamber, caused by ionizing collisions with the ions and electrons streaming from the source changed. The plasma potential of the induced background plasma increased from ~ 42 V to ~ 104 V, and the density of the induced background plasma doubled.

The increased plasma potential led to a reduction in beam energy due to the beam potential only increasing minutely, $\sim$1-2.5 V. This led to a decreased beam energy, down from 72-76 eV to 12-17 eV at the center of the beam. This was also accompanied by an 80% reduction in beam density at the higher pressures.

We found that the Langmuir probes produced plasma potentials that were more in line with the beam potentials detected with the RFEA probe, and we postulate that the discrepancy could in part be due to the Langmuir probe being unsuited to measuring the plasma potentials that close to the source, and we recommend using emissive probes for future works when measuring the plasma potential. We also found that the electron temperatures ranged between 2-5 eV for the radial positions corresponding to the aperture of the

separation grid.

The electron densities in the new configuration were found to vary densities ranging from $5 * 10^{15} m^{-3}$ at the lowest pressure to $9 * 10^{15} m^{-3}$ highest pressure at the 0 cm radial position.

We also found that the positively biased configuration produced an electron beam whose energy approached the potential difference between the anode cage and the cathode filaments as the pressure decreased, and the mean free path increased. We have postulated that this might provide a means of examining how effective the discharge current is at ionizing the neutral gas in the source.

8.1   Future work and outlook

As the change in grid potential was induced by a short-circuit between the anode cage and the separation grid we were unable to perform all experiments for both configurations. Repairing the source and separating grid and installing a power supply that is capable of producing grid potentials that are both negative and positive would allow us to perform experiments regarding positive grid potentials and comparing the effects to negative grid potentials.

The fact that we could only accurately discern the electron beam on the far end of the grid in the new configuration raises the question about how much of an effect the unevenness in the source has had on our measurements. We thus leave verifying that these electron beams are visible when all the filaments in the source are working optimally as a possible expansion of our work.

We also leave examining the axial and radial plasma potential profiles of our configurations using emissive probes as future work. This might be expedited if one was able to reconfigure the axial probe mount that is used with the helicon source to take axial measurements for the DC-source.

The results in this paper could be used in order to develop diagnostic tools for DC-discharge plasma sources that do not require the probe to be inserted into the plasma source. This might be useful in industrial applications when you want to determine if your source is working properly and the construction of said source does not allow for measurement devices to be inserted into the source chamber.

We also hope that this work can help expand the knowledge of double-layer plasma and how they can be manipulated. This work can also be used

as a point of further study when it comes to the effects of ion beams in double layer devices and how the physical separation mechanisms between the plasmas affects the propagation and generation of beams in the plasmas.

Bibliography

Aanesland, A., Fredriksen, Å., Byhring, H. S., and Gulbrandsen., N. (2016). Lab exercise no.4. Diagnostics with the retarding field energy analyzer (RFEA). Laboratory handout for the FYS-3017 Experimental Plasma Physics course, spring semester of 2016, University of Tromsø.

Armstrong, R. and Schrittwieser, R. (1991). Ion-beam-driven low-frequency instability at a probe in a double-plasma device. *Plasma Physics and Controlled Fusion*, 33(12):1407.

Barrett, P. J. and Greaves, R. G. (1989). Double-plasma instability near the ion plasma frequency. *Physics of Fluids B: Plasma Physics*, 1(9):1776–1779.

Böhm, C. and Perrin, J. (1993). Retarding-field analyzer for measurements of ion energy distributions and secondary electron emission coefficients in low-pressure radio frequency discharges. *Review of Scientific Instruments*, 64(1):31–44.

Byhring, H. S., Charles, C., Fredriksen, ., and Boswell, R. W. (2008). Double layer in an expanding plasma: Simultaneous upstream and downstream measurements. *Physics of Plasmas*, 15(10):102113.

Chen, F. F. (1984). *Introduction to Plasma Physics and controlled fusion*. Springer US, 2 edition. doi:10.1007/978-1-4757-5595-4.

Chen, F. F. (2003). Lecture Notes on Langmuir probe Diagnostics. http://www.seas.ucla.edu/ ffchen/Publs/Chen210R.pdf.

Chutia, J., Sato, S., Kubo, H., and Nakamura, Y. (1991). Low-frequency instability excited by a mesh grid in a double-plasma device. *Journal of Plasma Physics*, 46(3):463–471.

Davisson, C. and Germer, L. H. (1922). The Thermionic Work Function of Tungsten. *Phys. Rev.*, 20:300–330.

Fredriksen, Å., Mishra, L. N., and Byhring, H. S. (2010). The effects of downstream magnetic field on current-free double layers and beam formation in the Njord helicon plasma device. *Plasma Sources Science and Technology*, 19(3):034009.

Åge Skøelv (1981). Ionestrålediagnostikk ved hjelp av elektronmettet plan Langmuir probe [Norwegian]. Ion beam diagnostics using electron saturated planar Langmuir probe. Master's thesis, University of Tromsø.

Godyak, V. A., Piejak, R. B., and Alexandrovich, B. M. (1993). Probe diagnostics of non-Maxwellian plasmas. *Journal of Applied Physics*, 73(8):3657–3663.

Godyak, V. A., Piejak, R. B., and Alexandrovich, B. M. (2002). Electron energy distribution function measurements and plasma parameters in inductively coupled argon plasma. *Plasma Sources Science and Technology*, 11(4):525. http://stacks.iop.org/0963-0252/11/i=4/a=320.

Gulbrandsen, N. and Fredriksen, Å. (2017). RFEA Measurements of High-Energy Electrons in a Helicon Plasma Device with Expanding Magnetic Field. *Frontiers in Physics*, 5:2.

Gulbrandsen, N., Fredriksen, Å., Jr., J. C., and Scime, E. (2015). A comparison of ion beam measurements by retarding field energy analyzer and laser induced fluorescence in helicon plasma devices. *Physics of Plasmas*, 22(3):033505.

Gulbrandsen, N., Miloch, W. J., and Fredriksen, Å. (2013). Interpretation of Ion Velocity Distributions Measured with a Grounded Retarding Field Energy Analyzer (RFEA) in an inductively coupled helicon plasma. *Contributions to Plasma Physics*, 53(1):27–32.

Hershkowitz, N. (1985). Review of recent laboratory double layer experiments. *Space Science Reviews*, 41(3):351–391. doi: 10.1007/BF00190655.

Hershkowitz, N. (2005). Sheaths: More complicated than you think. *Physics of Plasmas*, 12(5):055502.

Hollenstein, C., Guyot, M., and Weibel, E. S. (1980). Stationary Potential Jumps in a plasma. *Physical Review Letters*, 45(26):2110–2113.

Lassner, E. and Schubert, W.-D. (1999). *Tungsten: Properties, Chemistry, Technology of the Element, Alloys, and Chemical Compounds*, volume 4 of *10*. Springer US, `http://www.springer.com/gp/book/9780306450532`, 1 edition. ISBN:978-1-4615-4907-9.

Lieberman, M. A. and Lichtenberg, A. J. (2005). *Principles of Plasma Discharges and Materials Processing, 2nd Edition*. Wiley, 2 edition. ISBN: 978-0-471-72001-0.

Magnus, F. and Gudmundsson, J. T. (2008). Digital smoothing of the Langmuir probe I-V characteristic. *Review of Scientific Instruments*, 79(7):073503.

Mazouffre, S. (2016). Electric propulsion for satellites and spacecraft: established technologies and novel approaches. *Plasma Sources Science and Technology*, 25(3):033002.

Miloch, W. J., Gulbrandsen, N., Mishra, L. N., and Fredriksen, Å. (2011). Ion velocity distributions in the sheath and presheath of a biased object in plasma. *Physics of Plasmas*, 18(8):083502.

Montgomery, D. and Joyce, G. (1969). Shock-like solutions of the electrostatic Vlasov equation. *Journal of Plasma Physics*, 3(1):1–11. doi:10.1017/S0022377800004141.

Osnes, S. (2016). Characterization of the DC Double-Plasma source in the Njord device at UiT. Project Paper in Space Physics at University of Tromsø.

Pécseli, H., Armstrong, R., and Trulsen, J. (1981). Experimental observations of ion phase-space vortices. *Physics Letters A*, 81(7):386 – 390.

Phelps, A. V., Greene, C. H., Burke, J. P., and Phelps, A. V. (2000). Collision cross sections for argon atoms with argon atoms for energies from 0.01 eV to 10 keV. *Journal of Physics B: Atomic, Molecular and Optical Physics*, 33(16):2965.

Pierre, T., Leclert, G., and Braun, F. (1987). Magnetized double-plasma device for wave studies. *Review of Scientific Instruments*, 58(1):6–11.

Roth, J. R. (1995). *Industrial Plasma Engineering: Volume 1: Principles.* CRC Press. ISBN 9780750303170.

Sabadil, H., Klagge, S., and Kammeyer, M. (1988). Langmuir probe measurements of axial variation of plasma parameters in 27.1 MHz rf oxygen planar discharges. *Plasma Chemistry and Plasma Processing*, 8(4):425–444. http://dx.doi.org/10.1007/BF01016058.

Sato, N., Sugai, H., and Hatakeyama, R. (1975). Spatial Evolution of Velocity-Modulated Ion Beams in a Plasma. *Phys. Rev. Lett.*, 34:931–934.

Stenzel, R. L., Williams, R., Agüero, R., Kitazaki, K., Ling, A., McDonald, T., and Spitzer, J. (1982). Novel directional ion energy analyzer. *Review of Scientific Instruments*, 53(7):1027–1031.

Taylor, R. J., Baker, D. R., and Ikezi, H. (1970). Observation of Collisionless Electrostatic Shocks. *Phys. Rev. Lett.*, 24:206–209.

Taylor, R. J., MacKenzie, K. R., and Ikezi, H. (1972). A Large Double Plasma Device for Plasma Beam and Wave Studies. *Review of Scientific Instruments*, 43(11):1675–1678. http://dx.doi.org/10.1063/1.1685522.

Tribulato, G. (2007). Characterization of a magnetized plasma in cylindrical geometry. Master's thesis, University of Tromsø. link: http://hdl.handle.net/10037/1202.

Weber, W. J., Armstrong, R. J., and Trulsen, J. (1979). Ion-beam diagnostics by means of an electron-saturated plane Langmuir probe. *Journal of Applied Physics*, 50(7):4545–4549.

Xiao, D. (2016). *Gas Discharge and Gas Insulation.*, volume 6 of *Energy and Environment Research in China*, chapter 3. Springer-Verlag Berlin Heidelberg. doi: 10.1007/978-3-662-48041-0_3.